STUDIES ON FUNCTIONALIZATION OF SELF-ASSEMBLED MONOLAYER ELECTRODE

（自己集合単分子膜を被覆した電極の機能化に関する研究）

1997

MASAYUKI OHTANI

Department of Applied Chemistry
Faculty of Engineering
Osaka University

Preface

The work of this thesis was carried out under the guidance of Professor Dr. Hiroshi Yoneyama at Department of Applied Chemistry, Faculty of Engineering, Osaka University from 1994 to 1996.

The aim of this thesis is to develop novel functionalized electrodes utilizing the self-assembly of molecules on gold substrates and to elucidate voltammetric behaviors of them. I hope that the findings obtained in this work will benefit in progress in interfacial electrochemistry.

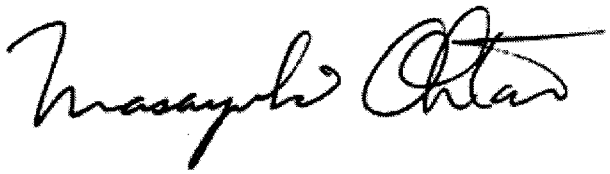

Masayuki Ohtani

Department of Applied Chemistry
Faculty of Engineering
Osaka University
Yamada-oka, Suita, Osaka 565, Japan

January / 1997

Contents

Chapter 3

Chapter 4

General Introduction

The self-assembled monolayer (SAM) is spontaneously formed by chemical adsorption of molecules onto a substrate from a homogeneous solution. The organization is obtained from the affinity of the head group for the substrate combined with the favorable interactions between close-packed tail groups. The first class of SAM is the monolayer of alkylsilanes formed on glass or aluminum oxide and the phenomenon of self-assembly has been known for nearly 50 years [W.C. Bigelow, D.L. Pickett, and W.A. Zisman, *J. Colloid Sci.*, **1**(1946)513.]. The second class of SAM is based on strong adsorption of thiols, disulfides, and related moieties onto several kinds of metals such as gold, platinum, and mercury. Recognition of this versatile approach can be credited to Allara and Nuzzo in 1983 [R.G. Nuzzo and D.L. Allara, *J.Am.Chem.Soc.*, **105**(1983)4481.], and the succeeding papers in 1987 by various groups initiated high activities for research on thiolate SAM, because SAM with sulfur moieties is more easily and reproducibly prepared than with the hydrolytically sensitive silanes.

This thesis deals with thiolate SAMs on Au substrate. The proposed reactions for both thiols and disulfides lead to formation of a gold(I)-thiolate species:

$$Au_n + RSH \rightarrow Au_{n-1}Au^+S^-{-}R + 1/2H_2$$

$$Au_n + 1/2RSSR \rightarrow Au_{n-1}Au^+S^-{-}R$$

No external oxidant or reductant is needed for self-assembly since SAMs can be formed even from the gas phase. Since SAMs of thiol and related moieties do possess a structural order and a high packing density due to the van der Waals forces, the monolayer displays a highly impermeable character toward both solvent and electrolyte ions. Using these qualities, electron transfers of a redox species at the SAM electrode with electron tunneling mechanism has been studied to investigate the effect of insulating layer of SAM on the rate of electron transfer reactions. Although such fundamental studies have been mostly carried out in electrochemistry fields, SAM electrodes are also useful for practical applications,

because SAM which contains functional group such as acid/base group and enzymatic activities can be prepared, as recent studies showed.

The present study has aimed to develop the novel functionalized electrodes utilizing thiolate SAM and elucidate the electrochemical characteristics of SAM-modified electrodes.

This thesis is consisted of four chapters. Chapter 1 and 2 describe simple techniques that allow preparation of a microelectrode array utilizing the photo-induced elimination of SAM in air and the removal of SAM in cyanide solution, respectively. SAM of a long alkylthiolate was used as an insulating material. Chapter 3 describes the preparation of functionalized electrode for electrochemical oxidation of NADH. The electrodes were prepared by using The SAM was used as an anchor to bind an electrocatalytic mediator for the NADH oxidation to an electrode surface. A theory on the voltammetric response of electrodes coated with electroactive monolayer is presented in Chapter 4, which gives theoretical basis for anomalous voltammetric behaviors of surface-confined redox species such as current spikes and broadning of redox waves. Finally, the results obtained in the present study are summarized in Conclusion.

List of Publications

1. Masayuki Ohtani, Tomohide Sunagawa, Susumu Kuwabata and Hiroshi Yoneyama, Preparation of a microelectrode array by photo-induced elimination of a self-assembled monolayer of hexadecylthiolate on a gold electrode, *J. Electroanal. Chem.*, 1995, **396**, 97-102.

2. Masayuki Ohtani, Susumu Kuwabata and Hiroshi Yoneyama, Electrochemical oxidation of reduced nicotinamide coenzymes at Au electrode modified with phenothiazine derivatives monolayer, *J. Electroanal. Chem.*, in press.(JEC4888)

3. Masayuki Ohtani, Tomohide Sunagawa, Susumu Kuwabata and Hiroshi Yoneyama, Preparation of a microelectrode array using desorption of a self-assembled monolayer of hexadecylthiolate on a gold electrode in cyanide solution, *J. Electroanal. Chem.*, in press.(JEC5017)

4. Masayuki Ohtani, Susumu Kuwabata and Hiroshi Yoneyama, Voltammetric response accompanied by inclusion of ion-pairs and triple ions formation of electrodes coated with an electroactive monolayer film, *Anal. Chem.*, in contribution.(AC960952G)

chapter 1

Preparation of a Microelectrode Array by Photo-induced Elimination of a Self-assembled Monolayer of Hexadecylthiolate on a Gold Electrode

1.1 INTRODUCTION

In the past several years much attention has been paid to a self-assembled monolayer of alkylthiolate derivatives on gold surface which is formed by chemisorption of dissolved alkylthiols and their spontaneous organization [1]. Beside fundamental studies on the structure of the monolayers [2-6], some applications such as information storage devices [7], chemical sensors [8], lithography [9], and resists for patterned etching of Au and Si [10] have been attempted. In electrochemical fields, gold electrodes coated with the self-assembled monolayer have been used for fundamental studies on long range electron transfers [11-17]. Electrochemical techniques were successfully applied to detect structural defects of the monolayer like pinholes [11,18-22]. Furthermore, preparation of metal electrodes coated with the monolayers of thiolates having electrochemically active groups has attracted interests as a new method to attach special functions to the electrodes [23-27]. These utilizations are indebted to relatively high stability of the self-assembled monolayer against mechanical, thermal, and chemical treatments. Recently, it has been reported that irradiation of the alkylthiolates monolayer in air with UV-lights induces oxidation to the corresponding alkylsulfonates, and the oxidized monolayer is easily removed from the gold substrate surface when immersed in aqueous solution [28-31]. If UV lights through a photomask are irradiated to the monolayer, patterned elimination takes place, and this property has been successfully utilized as a photoresist [32].

This chapter describes the attempt of preparation of the microelectrode array by utilizing the

photo-induced elimination of alkanethiolate from Au electrode in electrolyte solutions as well as in air. Beside the removal of the monolayer by irradiation with UV lights in air, it has been discovered that a self-assembled monolayer of hexadecylthiolate on Au surface is eliminated by irradiating the monolayer with visible lights in electrolyte solution containing $K_4Fe(CN)_6$. In this chapter, voltammetric properties of various photo-fabricated electrodes are presented and discussed.

1.2 EXPERIMENTAL SECTION

Ethanol used as a solvent was distilled after storing in the presence of sodium metal. Water used for preparation of electrolyte solutions was purified by twice distillation of deionized water. Other chemicals of reagent grade were used without further purification. An Au plate (0.5 x 0.5 cm) was used as an electrode substrate. An electrical lead wire was attached to its back face with silver epoxy and fixed with epoxy resin. The surface of the electrode was successively polished with 1.0 and 0.3 μm alumina, followed by being subjected to ultrasonication in water. Formation of a self-assembled monolayer of hexadecylthiolate on the Au electrode substrate was carried out by immersing the electrode in ethanolic solution containing 1 mmol dm^{-3} hexadecylthiol for 12 h, and then the electrode was rinsed several times with pure ethanol to remove physically adsorbed species. The resulting electrode will be denoted here as HDT/Au.

Photo-induced elimination of hexadecylthiolate adsorbed on the Au electrode was made by irradiation of the entire surface of HDT/Au with a 500 W high pressure Hg arc lamp (Ushio UI-501C) in air or in 0.5 mol dm^{-3} KCl aqueous solution containing 50 mmol dm^{-3} $K_4Fe(CN)_6$. The light intensity used was 800 mW cm^{-2}. In the case of preparation of an ordered microelectrodes array in the HDT/Au electrode in air, the Hg arc lamp was irradiated to the electrode surface through a photomask (Toppan Printing Co.) prepared by photorithography. The mask had transparent holes of 19 μm radius arrayed with regular hexagonal bases. The distance between the centers of neighboring holes was 76 μm, giving a ratio of transparent part to opaque one of 1:3. Focused photo-induced elimination of hexadecylthiolate from HDT/Au was made by one-pulse irradiation in the above mentioned electrolyte solution using second harmonic of a Q-switched Nd:YAG laser

(532 nm) (Spectra-Physics GCR-11). The light intensity of the focus was 20 mW and the half-width of pulse was 10 ns.

Electrochemical measurements were carried out using a BAS-100B electrochemical work-station. An Ag/AgCl(KCl-saturated) served as a reference electrode and a Pt foil (2 x 3 cm^2) was used as a counter electrode. Above mentioned electrolyte solution was used in this study and the solution was bubbled with N_2 for 1 h prior to measurements.

1.3 RESULTS AND DISCUSSION

1.3.1 Photo-induced Elimination of Self-assembled Hexadecylthiolate on an Au Surface in Air

The entire surface of a HDT/Au electrode was irradiated in air for different time with a 500 W high pressure Hg arc lamp, and after then cyclic voltammograms were taken in 50 mmol dm^{-3} $K_4[Fe(CN)_6]$ dissolved in 0.5 mol dm^{-3} KCl aqueous solution. Figure 1.1 shows results obtained for the electrodes irradiated for 0, 2, 3, and 4 h. The as-prepared HDT/Au electrode exhibited no electrochemical response, whereas anodic and cathodic waves due to the redox reaction of $[Fe(CN)_6]^{3-/4-}$ appeared and increased with increasing the irradiation time. The cyclic voltammogram of the electrode taken after irradiation for 4 h was almost consistent with that of the bare Au electrode in the same electrolyte solution, indicating that UV-irradiation for 4 h was

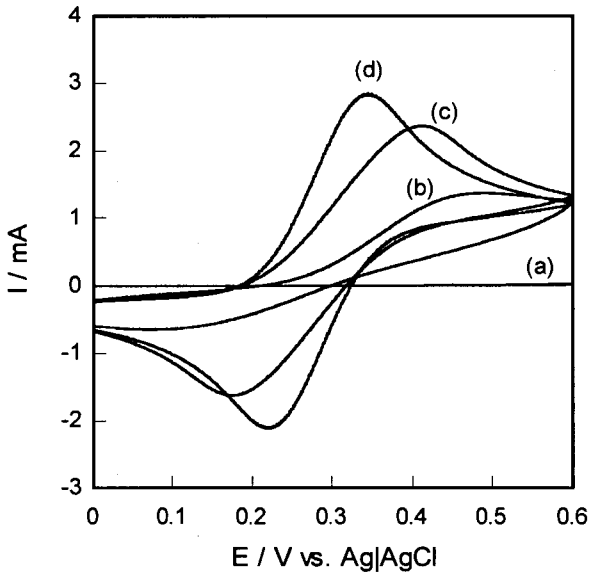

Figure 1.1

Cyclic voltammograms of HDT/Au electrode taken in 50 mmol dm^{-3} $K_4[Fe(CN)_6]$ dissolved in 0.5 mol dm^{-3} KCl solution at $v = 100$ mV s^{-1}. The measurements were made after irradiation of the electrode in air with a 500 W Hg arc lamp for 0 (a), 2 (b), 3 (c), and 4 (d) h.

enough to remove completely the hexadecylthiolate adsorbed on the Au electrode. As shown in Figure 1.1, the cyclic voltammogram of the HDT/Au electrode irradiated for less than 4 h showed a large peak separation the magnitude of which depends on the irradiation time, and the longer the irradiation time, the smaller the peak separation. Such behaviors may reflect effects of different magnitude of *IR* drops at the diffusion layer on cyclic voltammogram of an electrode of conventional size. In the case of UV-irradiation of the electrode in air, oxidation of the adsorbed hexadecylthiolate must uniformly take place on the entire electrode surface, but the photo-oxidation proceeds slowly and then the removal of the closely packed monolayer would take place in such way as to give isolated islands of the adsorbed molecules. With increasing the illumination time, the density of the adsorbed hexadecylthiolate must become low. Even if the density becomes such low that adsorbed molecules cannot interact with each other, however, cyclic voltammograms do not exhibit the characteristic feature of microelectrode array, due probably to contribution of a fairly large *IR* drop across the covered molecules to the cyclic voltammograms of the resulting electrode.

1.3.2 Preparation of an Ordered Microelectrode Array by Irradiation of UV Lights through a Photomask

The HDT/Au electrode was irradiated in air with the Hg arc lamp through the photomask mentioned in the experimental section to prepare ordered microelectrode array on the electrode. Cyclic voltammograms of the resulting electrode were taken in the $[Fe(CN)_6]^{4-}$ solution, and the results obtained are shown in Figure 1.2. In this figure, dimensionless current, $I/FAc^*D^{1/2}(F/RT)^{1/2}v^{1/2}$ [33, 34], is given in the vertical axis to compare the shape of voltammograms taken at different potential sweep rates, where A is the area of electrode substrate, c^* is the bulk concentration of electrochemically active substances, D is the diffusion coefficient for $[Fe(CN)_6]^{4-}$ (6.8×10^{-6} cm^2 s^{-1} [34]), v is the potential sweep rate, F, R and T are their usual significance. The voltammogram obtained at 20 mV s^{-1} showed definite anodic and cathodic peak currents, whereas the peak height became lower with increase in the potential sweep rate, making its shape sigmoidal like the *I-E* curve obtained for the single microelectrode. These electrochemical responses are characteristics

of the microelectrodes array [18,34,35]. Theoretical studies on the microelectrodes array [18, 34,35] gave the dimensionless currents ψ of cyclic voltammograms as given by eq (1.1)

$$\psi = I/[nFc^*(nFDv/RT)^{1/2}] \quad (1.1)$$

where I is the current density, c^* is the bulk concentration of redox active species, D is the diffusion coefficient of electroactive species, and v is the potential scan rate. ψ is also given as the solution of the following integral equation.

$$\psi = Ae^{\alpha\varepsilon}[(1-\mathbf{I}\psi - \psi/B) - (\mathbf{I}\psi + \psi/A)e^{-\varepsilon}] \quad (1.2)$$

where $\mathbf{I}\psi$ is the convolution integral of ψ given by eq (1.3), ε is dimensionless potential given by eq (1.4), and A and B are defined by eqs (1.5) and (1.6).

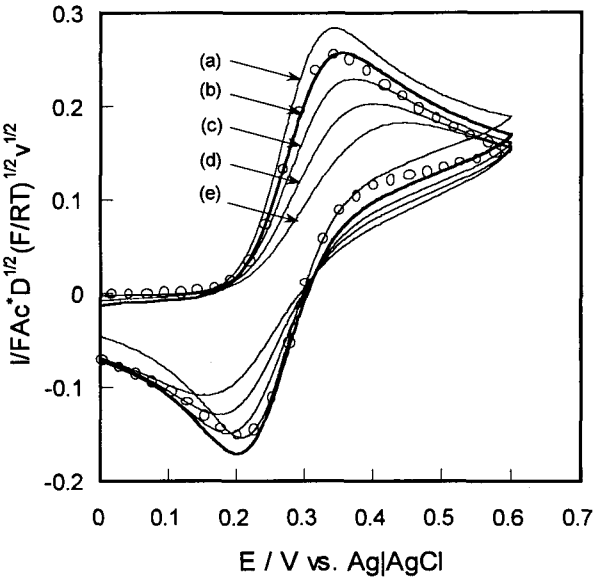

Figure 1.2

Cyclic voltammograms of HDT/Au electrode irradiated with a Hg arc lamp though a photomask in air. v = 20 (a), 50 (b), 200 (c), 500 (d), and 1000 (e) mV s^{-1}. The open circles are simulated plots of a cyclic voltammogram taken at 50 mV s^{-1} using eq (1.1) in text.

$$\mathbf{I}\psi = \pi^{-1/2}\int_0^t \psi(t-\tau)d\tau \quad (1.3)$$

$$\varepsilon = -(nF/RT)(E-E^{o\prime}) \quad (1.4)$$

$$A = k^o(1-\theta)(RT/DFv)^{1/2} \quad (1.5)$$

$$B = (DRT(1-\theta)/Fv)^{1/2}/(0.6r_h) \quad (1.6)$$

The A and B are dimensionless parameters including the heterogeneous electron transfer rate constant (k^o), a half of the average distance between the centers of neighboring microelectrodes (r_h), and a ratio of inactive area (θ), and other parameters have their usual significance. By substituting k^o = 0.0125 cm s^{-1} [34], r_h = 38 μm and θ = 0.75 which are given by the photomask used into equations (1.3) and (1.4), simulated plots of a cyclic voltammogram taken at 50 mV s^{-1} were obtained, as shown by open circles in Figure 1.2. Good agreements are seen between the simulated

plots and the experimentally obtained voltammogram, indicating that the photomask pattern was precisely produced on the HDT/Au electrode.

1.3.3 Photo-induced Elimination of Self-assembled Hexadecylthiolate on an Au Surface in Electrolyte Solution

It was found that the photo-induced elimination of the thiolate monolayer also occurred in the above mentioned electrolyte solution. Figure 1.3 shows changes in cyclic voltammograms of the HDT/Au electrode which was irradiated with the Hg arc lamp under open circuit conditions for various times prior to the measurements. The increase in the redox waves with increase in the illumination time is also seen in this case. It is noteworthy by comparing the results shown in Figure 1.3 with Figure 1.1 that the rate of the photo-induced elimination in the electrolyte solution was higher than that in air. The same Hg lamp was used for both cases, but since the irradiation of the electrode in the electrolyte solution does not allow the photon incidence of wavelength shorter than 420 nm at the electrode surfaces due to high absorbance of dissolved $[Fe(CN)_6]^{4-}$ species, it is believed that visible lights worked effectively for the elimination of hexadecylthiolate on the Au electrode. Indeed, similar increase in the redox waves was observed when the HDT/Au electrode

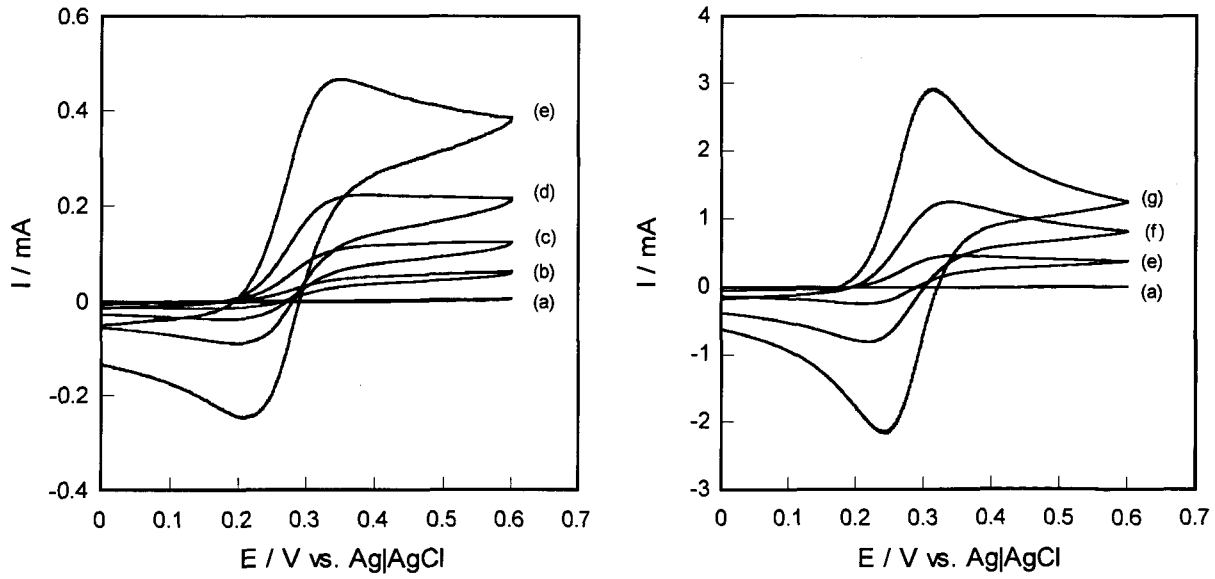

Figure 1.3

As in Figure 1.1 but the irradiation was made for 0 (a), 20 (b), 30 (c), 40 (d), 50 (e), 60 (f), and 70 (g) min to the electrode immersed in the electrolyte solution under the open circuit condition.

was irradiated in the electrolyte solution with the second harmonic of a Nd:YAG laser at 532 nm. In contrast, the photo-induced oxidation of hexadecylthiolate in air needs UV lights, suggesting that the mechanism of photo-induced elimination of hexadecylthiolates is different between in air and in electrolyte solution. If the photo-induced elimination of hexadecylthiolates with use of the Hg arc lamp was also attempted by irradiating the HDT/Au electrode immersed in 0.5 mol dm^{-3} KCl solution or distilled water in the absence of $[Fe(CN)_6]^{4-}$, the observed rate of the elimination was lower than that obtained for the irradiation of the electrode in air shown in Figure 1.1, suggesting that $[Fe(CN)_6]^{4-}$ dissolved in the electrolyte solution was involved in cleavage of S-Au bonding. The mechanism for the cleavage and the role of $[Fe(CN)_6]^{4-}$ will be described in chapter 2.

As already shown in Figure 1.3, irradiation of the entire surface of the HDT/Au electrode immersed in the $[Fe(CN)_6]^{4-}$ solution caused gradual elimination of hexadecylthiolate from the Au surface. It was found that in a middle stage of the photo-induced elimination of the monolayer on Au electrode the electrode possessed electrochemical properties characteristics of the microelectrodes array. If the irradiation time was shorter than 40 min, the resulting electrode gave sigmoidal curves, which are a characteristic property of microelectrodes that appear when the radial diffusion layer developed at each micro electrode is isolated from each other. When the irradiation time was longer than 40 min, both anodic and cathodic peak waves developed in the cyclic voltammograms. In that case, the peak height was decreased by increasing the potential sweep rate as shown in Figure 1.4 where the voltammograms taken after irradiation for 60 min are given. The obtained results are in conformity with whose obtained at microelectrode array. When cyclic voltammogram of the electrode is taken at a lower potential sweep rate, the radial diffusion layers developed at each microelectrode sur-

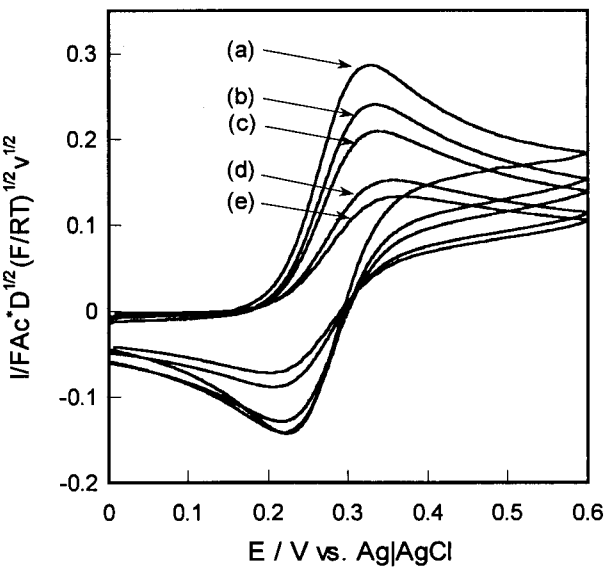

Figure 1.4

Cyclic voltammograms of the HDT/Au electrode taken after irradiation of the electrode for 60 min with a Hg arc lamp in the electrolyte solution. v = 20 (a), 50 (b), 100 (c), 500 (d), and 1000 (e) mV s^{-1}.

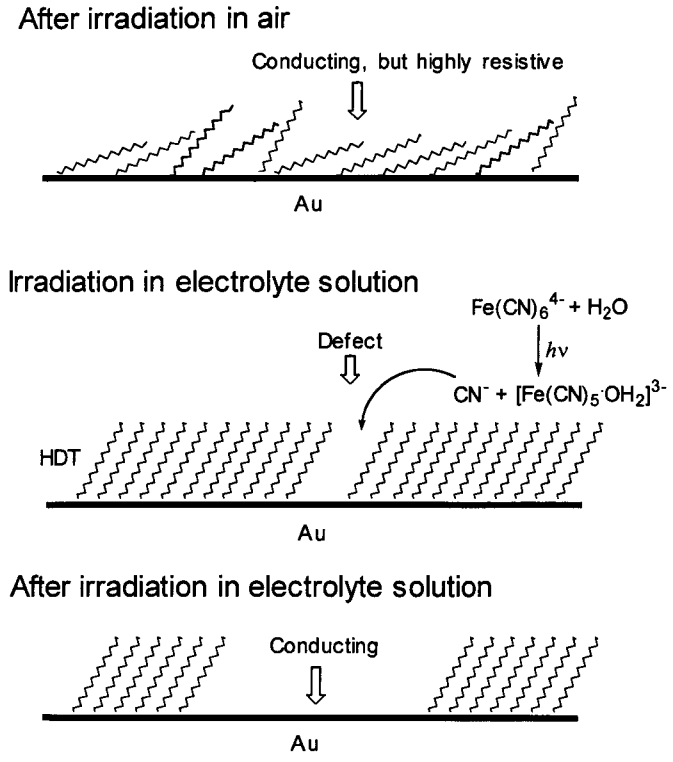

Figure 1.5

Schematic illustrations of the formation of microelectrode in the HDT/Au electrode.

face are overlapped with each other, resulting in formation of a planar diffusion layer. The voltammogram profile obtained under such condition resembles that obtained using a planar electrode having a large size, though the ratio of Faradaic currents to background currents is much higher than that obtained at a planar electrode. With increase in the potential sweep rate the size of the radial diffusion layer reduces, causing their loose overlapping. As shown in Figure 1.1, however, if the HDT/Au electrode was irradiated in air with UV light for different time, no electrochemical responses characteristics of the microelectrodes array appeared.

If the irradiation was carried out in the electrolyte solution, $[Fe(CN)_6]^{4-}$ close to the S-Au bonding is believed to assist the bond-cleavage, and this event occurs at the place where structural defects of the self-assembled monolayer are present, because closed packing of the adsorbed layer does not allow insertion of any kind of molecule into the monolayer. Once the exposed area appears with irradiation, elimination of the adsorbed molecule with assistance by $[Fe(CN)_6]^{4-}$ becomes promoted, resultong in microelectrodes array. In Figure 1.5, hypothetical illustrations for the formation of microelectrodes in the electrolyte solution are given together with that for the photo-elimination of the monolayer in air.

1.3.4 Preparation of Microelectrodes in Electrolyte Solution

One pulse of a focused laser beam from the Nd:YAG laser was irradiated to the HDT/Au electrode immersed in the $[Fe(CN)_6]^{4-}$ solution, and then cyclic voltammograms of the resulting electrode were taken at various potential sweep rates. The diameter of the laser spot irradiated on

the HDT/Au electrode was evaluated to be about 180 μm by its observation with a microscope. The obtained results are shown in Figure 1.6. The voltammograms taken at potential sweep rates lower than 10 mV s^{-1} gave a sigmoidal *I-E* curve the shape of which and a limiting plateau current (I_{lim}) were independent on the potential sweep rate, giving a characteristic feature of a single microelectrode. The relationship between I_{lim} and radius of the electrode (r) in an one-electron system is given by

$$I_{lim} = 4rFDc^* \qquad (1.7)$$

By substituting the known parameters and experimentally determined I_{lim} = 1.2 μA into equation (1.7), the radius of the prepared electrode was evaluated to be 91 μm which agrees well with that of the light spot as described above. When the potential sweep rate was increased, gradual increase in anodic and cathodic peak waves was observed, indicating that the diffusion mode changes from radial into planar one. This is another electrochemical feature of the microelectrode.

Plural microelectrodes were successfully prepared on the HDT/Au by irradiation in the electrolyte solution of the laser spot at ordered places in 0.5 mm distance of the electrode sur-

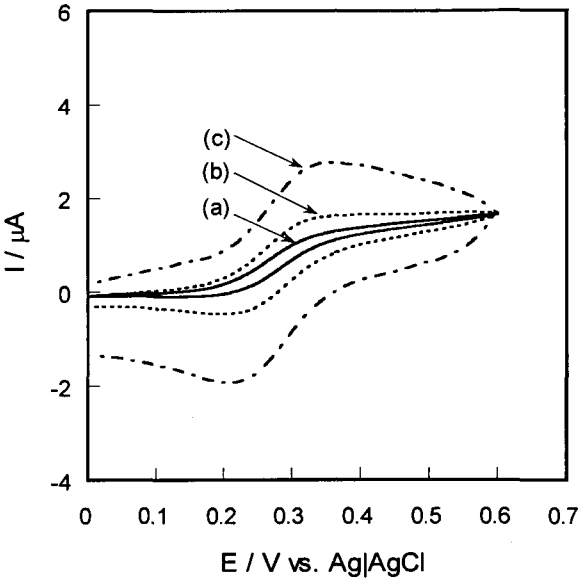

Figure 1.6

Cyclic voltammograms of the HDT/Au electrode irradiated with a laser spot of ca. 90 μm radius prior to measurements. v = 10 (a), 100 (b), and 500 (c) mV s^{-1}

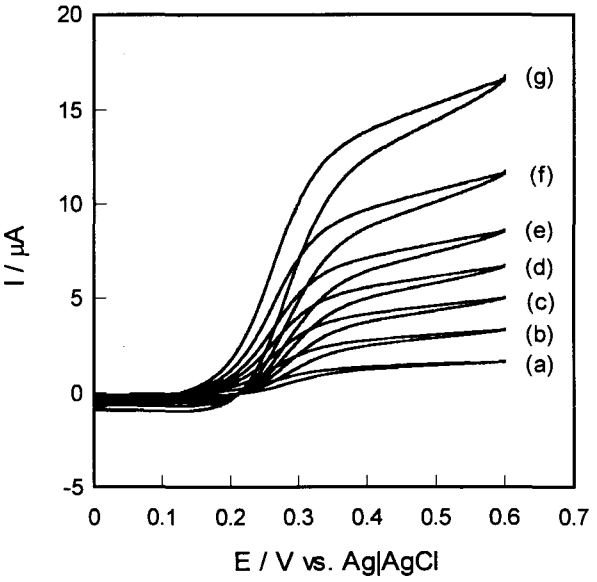

Figure 1.7

Cyclic voltammograms of the HDT/Au electrode in which plural microelectrodes were prepared by one-pulse irradiation of laser spots of ca. 90 μm radius at different places of the electrode surface. The number of the microelectrodes prepared was 1 (a), 2 (b), 3 (c), 4 (d), 5 (e), 7 (f), and 10 (e). v = 10 mV s^{-1}

face. Figure 1.7 shows changes in cyclic voltammograms caused by increase in the number of the microelectrodes. As expected, I_{lim} increased in proportion to the number of the microelectrodes, while the sigmoidal shape of *I-E* curve was retained, suggesting that this technique is useful for preparation of plural microelectrodes.

1.4 REFERENCES

1. A. Ulman, An Introduction to Ultrathin Organic Films, Academic Press, San Diego, 1991, Part Three, and the references cited in there.
2. R. G. Nuo, L. H. Dubois and D. L. Allara, *J. Am. Chem. Soc.*, **112** (1990) 558.
3. L. Strong and G. M. Whitesides, *Langmuir*, **4** (1988) 546.
4. C. E. Chidsey, G. Liu, P. Rowntree and G. Scoles, *J. Phys.Chem.*, **91** (1989) 4421.
5. C. A. Widrig, C. A. Alves and M. D. Porter, *J. Am. Chem. Soc.*, **113** (1991) 2805.
6. C. A. Alves, E. L. Smith and M. D. Prter, *J. Am. Chem. Soc.*, **114** (1992)1222.
7. J. D. Swalen, D. L. Allara, J. D. Andrade, E. A. Chandross, S. Garoff, J. Isaelachvili, T. J. McCarthy, R. Murray, R. F. Pease, J. F. Rabolt and K. J. Wynne, *Langmuir,* **3** (1987) 932.
8. A. Kumar and G. M. Whitesides, *Science*, **263** (1994) 60.
9. A. Kumar and G. M. Whitesides, *Appl. Phys. Lett.*, **63** (1993) 2002.
10. N. L. Abbottt, A. Kumar and G. M. Whitesides, *Chem. Mater.*, **6** (1994) 596.
11. H. O. Finklea, S. Avery, M. Lynch, T. Furtsch, *Langmuir*, **3** (1987) 409.
12. H. O. Finklea and D. D. Hanshew, *J. Am. Chem. Soc.*, **114** (1992) 3173.
13. H. O. Finklea, M. S. Ravenscroft and D. A. Snider, *Langmuir*, **9** (1993) 223.
14. C. E. D. Chidsey, C. R. Bertozzi, T. M. Putvinski, A. M. Mujsce, *J. Am. Chem. Soc.*, **112** (1990) 4301.
15. C. E. D. Chidsey, *Science*, **251** (1991) 919.
16. C. Miller, P. Cuendet and M. Gratzel, *J. Phys. Chem.*, **95** (1991) 877.
17. C. Miller and M. Gratzel, *J. Phys. Chem.*, **95** (1991) 5225.

18. H. O. Finklea, D. A. Snider, J. Fedyk, E. Sabatani, Y. Gafni and I. Rubinstein, *Langmuir*, **9** (1993) 3660.
19. E. Sabatani and I. Rubinstein, *J. Phys. Chem.* **91** (1987) 6663.
20. E. Sabatani and I. Rubinstein, *J. Electroanal. Chem.*, **219** (1987) 365.
21. I. Rubinstein, S. Steinberg, Y. Tor, A. Shanzer, J. Sagiv, *Nature* **332** (1988) 426.
22. M. D. Porter, T. B. Bright, D. Allara, C. E. D. Chidsey, *J. Am. Chem. Soc.*, **109** (1987) 3559.
23. W. R. Fawcett, *J. Electroanal. Chem.*, **378** (1994) 117.
24. D. M. Collard and C. N. Sayre, *J. Electroanal. Chem.* **375** (1994) 367.
25. T. Ohtsuka, Y. Sato and K. Uosaki, *Langmuir*, **10** (1994) 3658.
26. K. Shimazu, I. Yagi, Y. Sato and K. Uosaki, *J. Electroanal. Chem.* **372** (1994) 117.
27. X. Tang, T. Schneider and D. A. Buttry, *Langmuir*, **10** (1994) 2235.
28. M. J. Tarlov, D. R. F. Burgess, Jr. and G. Gillen, *J. Am. Chem. Soc.*, **115** (1993) 5305.
29. Y. Li, J. Huang, R. T. McIver, Jr and J. C. Hemminger, *J. Am. Chem. Soc.*, **114** (1992) 2428.
30. J. Huang and J. C. Hemminger, *J. Am. Chem. Soc.*, **115** (1993) 3342.
31. J. Huang, D. A. Dahlgren and J. C. Hemminger, *Langmuir*, **10** (1994) 626.
32. S. Ching, R. Dudek and E. Tabet, *J. Chem. Edu.*, **71** (1994) 602.
33. T. Gueshi, K. Tokuda and H. Matsuda, *J. Electroanal. Chem.*, **89** (1978) 247.
34. T. Gueshi, K. Tokuda and H. Matsuda, *J. Electroanal. Chem.*, **101** (1979) 29.
35. J. Cassidy, J. Ghoroghchaian, F. Sarfarazi, J. J. Smith and S. Pons, *Electrochim. Acta*, **31** (1986) 629.

chapter 2

Preparation of a Microelectrode Array Using Desorption of a Self-assembled Monolayer of Hexadecylthiolate on a Gold Electrode in Cyanide Solution

2.1 INTRODUCTION

Recently, intensive studies have been carried out on the preparation and utilization of a self-assembled monolayer (SAM) of thiol or disulfide derivatives, which is formed by their chemisorption onto gold surface with spontaneous organization [1-3]. The SAM of long alkylthiolates possesses high stability [1,4] and the characteristics of insulator films [5,6]. Several attempts have been made to eliminate such an SAM from the Au substrate by using mechanical [7-9] and photo-oxidative [10-16] methods to make patterned holes in the SAM with the aim of applications as resist materials. In chapter 1 it is described that photo-induced desorption of SAM using three different techniques was useful for preparation of a microelectrodes array [17]; Irradiation of the Au electrode coated with hexadecylthiolate (HDT/Au) with UV-light through a photomask, two dimensional irradiation of the same electrode with a focused laser beam of 90 μm diameter in 0.5 mm distance, and irradiation of the entire surface of the HDT/Au electrode with UV light in a $K_4[Fe(CN)_6]$ aqueous solution. In the last case, the adsorbed hexadecylthiolate was found to be photo-desorbed in such a way as to give electrodes having electrochemical responses characteristic of a microelectrode array. However, the mechanism of the photodesorption of hexadecylthiolate was unclear when the last technique was developed. The study which is described in this chapter was initiated to clarify the role of $K_4[Fe(CN)_6]$ in the photo-induced elimination of the hexadecylthiolate that produced a microelectrode array at the HDT/Au electrode. As will be shown later, CN^- ions generated by photo-decomposition of $K_4[Fe(CN)_6]$ are found to be involved in the

desorption of the adsorbed hexadecythiolate from the gold surface, and attempts have been made to prepare microelectrodes array by just immersing the HDT/Au in aqueous cyanide solutions. The results obtained with such an approach will be described in this chapter.

2.2 EXPERIMENTAL SECTION

Ethanol used as a solvent was distilled after storing in the presence of sodium metal to eliminate water completely. Water used for preparation of electrolyte solutions was purified by twice distillation of deionized water. Other chemicals of reagent grade were used without further purification. An Au plate (0.5 x 0.5 cm^2) was used as the electrode substrate. An electrical lead wire was attached to its back face with silver epoxy and covered with epoxy resin. The surface of the electrode was polished successively with 1.0 and 0.3 mm alumina, followed by being subjected to ultrasonication in water. Formation of a SAM of hexadecylthiolate on the Au electrode substrate was carried out by immersing the electrode in ethanol containing 1 mmol dm^{-3} hexadecylthiol (Wako) for 12 h, and then the electrode was rinsed several times with ethanol to remove physically adsorbed species. The resulting electrode will be denoted here as HDT/Au electrode. The HDT/Au electrode was immersed either in a $K_4[Fe(CN)_6]$ solution pre-irradiated with a 500 W high pressure Hg arc lamp (Ushio UI-501C) or in a KCN aqueous solution to investigate the desorption behavior of the SAM. Both solutions were thermostated at 25±1 °C and saturated with N_2 gas for 30 min prior to use. Details of the experimental conditions are described in the Results and Discussion section.

Electrochemical measurements of the electrode was carried out in 50 mmol dm^{-3} (Wako) dissolved in 1 mol dm^{-3} KCl aqueous solution under thermostated conditions at 25±1 °C with the use of a BAS-100B electrochemical analyzer connected to a Gateway 2000 computer. An Ag|AgCl|KCl(sat) and a Pt foil (2 x 3 cm^2) served as a reference and a counter electrode, respectively. N_2 gas was thoroughly bubbled into the electrolyte solution prior to measurements.

To confirm the formation of microelectrodes array in SAM, electrodeposition of Cu was attempted for the HDT/Au electrode after immersing in KCN solution for a given time. For this

purpose, the electrode was polarized at -0.5 V vs. Ag|AgCl in 0.5 mmol dm^{-3} $CuSO_4$ aqueous solution for 10 s using an HA-301 potentiostat (HOKUTO DENKO Ltd.). The surface of the resulting electrode was observed by an optical microscope (Nikon, model S).

2.3 RESULTS AND DISCUSSION

2.3.1 Photo-induced Elimination of Self-assembled Hexadecylthiolate on an Au Surface in $K_4[Fe(CN)_6]$ solution

It was shown in chapter 1 that a SAM of hexadecylthiolate formed on an Au electrode was eliminated by illuminating the HDT/Au electrode with UV-light in 50 mmol dm^{-3} $K_4[Fe(CN)_6]$ dissolved in 0.5 mol dm^{-3} KCl aqueous solution [17]. Although the presence of $K_4[Fe(CN)_6]$ in the solution was found to be essential, its role in the elimination of the SAM was unclear. According to Ohno [18], illumination of $K_4[Fe(CN)_6]$ dissolved in aqueous solution with UV-light causes its decomposition to give CN^- ions, as given by

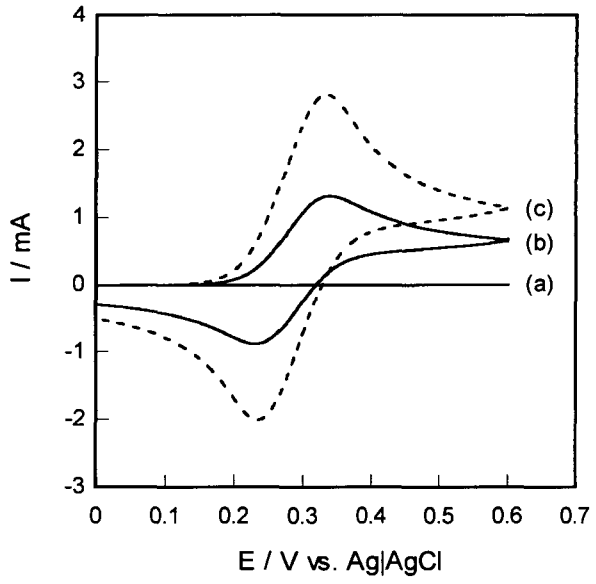

Figure 2.1

Cyclic voltammograms taken in 1 mol dm^{-3} KCl aqueous solution containing 50 mmol dm^{-3} $K_4[Fe(CN)_6]$ at the scan rate of 100 mV s^{-1}. (a) as-prepared HDT/Au electrode; (b) HDT/Au electrode prepared by immersing in 50 mmol dm^{-3} $K_4[Fe(CN)_6]$ solution for 1 h in dark after irradiation of the solution with an Hg arc lamp for 1h; (c) bare Au electrode.

$$[Fe(CN)_6]^{4-} + H_2O \xrightarrow{h\nu} [Fe(CN)_5OH_2]^{3-} + CN^- \qquad (2.1)$$

The involvement of the photoproduced CN^- ions in the elimination of the adsorbed hexadecylthiolate was confirmed by the following experiments. 50 mmol dm^{-3} $K_4[Fe(CN)_6]$ dissolved in 1 mol dm^{-3} KCl aqueous solution was irradiated with a 500 W high pressure Hg arc lamp for 1 h beforehand, and then the HDT/Au

electrode was immersed in that solution for 1 h in the dark, followed by thoroughly washing with distilled water. If a cyclic voltammogram of the resulting electrode was taken in a fresh solution of 50 mmol dm^{-3} $K_4[Fe(CN)_6]$ dissolved in 1 mol dm^{-3} KCl aqueous solution, the electrode showed activities for the redox reaction of $[Fe(CN)_6]^{3-/4-}$, as shown by curve (b) of Figure 2.1. In this figure, voltammograms of an as-prepared HDT/Au electrode and of a bare Au electrode were also shown. The as-prepared HDT/Au electrode exhibited no electrochemical response because of the high resistance of the SAM of hexadecylthiolate [5,6]. The finding that the HDT/Au electrode showed redox activity after soaking in the photo-irradiated $K_4[Fe(CN)_6]$ solution suggests that the photo-generated CN^- ions caused desorption of hexadecylthiolate chemisorbed on the Au electrode and that the irradiation of the HDT/Au electrode was not essential to desorb the adsorbed hexadecylthiolate. The results obtained here are in conformity with our previous report [17] that the immersion of Au electrodes coated with the same kind of SAM in aqueous solution containing CN^- caused desorption of the adsorbed thiolate.

2.3.2 Elimination of Self-assembled Hexadecylthiolate on an Au Surface in KCN Aqueous Solution

In our previous study [17], it was discovered that illumination of the entire surface of the electrochemically inactive HDT/Au electrode with UV-light from high pressure Hg lamp in $K_4[Fe(CN)_6]$ solution resulted in electrochemically active electrodes having the characteristic features of a microelectrodes array. If the adsorbed hexadecylthiolate is desorbed with assistance of the photogenerated CN^- as mentioned above, a similar microelectrode array could be prepared just by immersing the HDT/Au electrode in an aqueous cyanide solution. Gradual desorption of the adsorbed hexadecylthiolate was certainly suggested from changes in cyclic voltammograms of $K_4[Fe(CN)_6]$ at the HDT/Au electrode prepared by changing the soaking time of the electrode in 0.3 mol dm^{-3} KCN aqueous solution. As clearly shown in Figure 2.2, the redox waves due to $[Fe(CN)_6]^{3-/4-}$ became larger as the soaking time of the HDT/Au in the KCN solution increased. The difference between cathodic and anodic peak potentials decreased a little with the growth of the cyclic voltammograms.

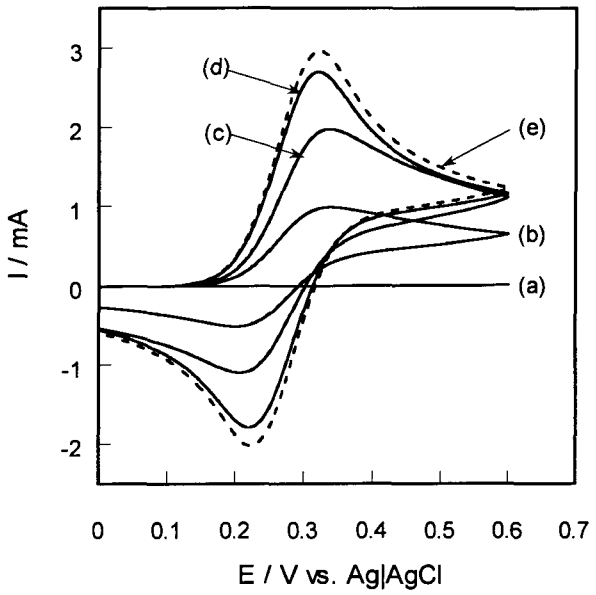

Figure 2.2

Cyclic voltammograms taken in 1 mol dm^{-3} KCl aqueous solution containing 50 mmol dm^{-3} $K_4[Fe(CN)_6]$ at 100 mV s^{-1}. The measurements were taken after soaking of the HDT/Au electrode into 0.3 mol dm^{-3} KCN aqueous solution for (a) 0 min, (b) 10 min, (c) 20 min, and (d) 30 min. The cyclic voltamogram of (e) was obtained at a bare Au electrode.

In order to obtain direct information on the formation of the microelectrode array in the HDT/Au electrode by the KCN soaking, attempts were made to deposit Cu onto the HDT/Au electrode after soaking the electrode in 0.3 mol dm^{-3} KCN solution for 20 min and then to observe the deposited Cu patterns. Figure 2.3(A) shows a picture taken by an optical microscope of the deposited Cu patterns on the HDT/Au electrode. The deposited Cu is given by dark spots in the picture, which are distributed over the whole surface of the HDT/Au electrode. By determining the diameter of all the Cu deposits on the HDT/Au electrode, a size-distribution profile of the deposited copper islands as shown in Figure 2.3.1 was obtained. The Cu deposits ranged from 11 to 21 μm in the radius, the average being 17 μm. If the area of the deposited Cu was determined and if its fraction to the total electrode area was evaluated, the fraction of Cu deposits of 0.25 was obtained.

Concerning the mechanism of the desorption of the adsorbed thiolate, we speculate like this; Cyanide ions enter into defects (pinholes) in the monolayer of hexadecylthiolate, since hydrophilic CN^- anions cannot penetrate the hydrophobic compact layer of the adsorbed hexadecylthiolate. Once the cyanide ions reach the Au electrode substrate, the desorption of the adsorbed hexadecylthiolate begins to take place at the pinhole. The size of the pinhole begins to grow with increasing the soaking time of the electrode in the KCN solution . The desorption of the adsorbed thiolate might occur as a substitution reaction with CN^- ions [19], but there is another possibility that the desorption takes place where the gold substrate is etched chemically with CN^- ions [20,21].

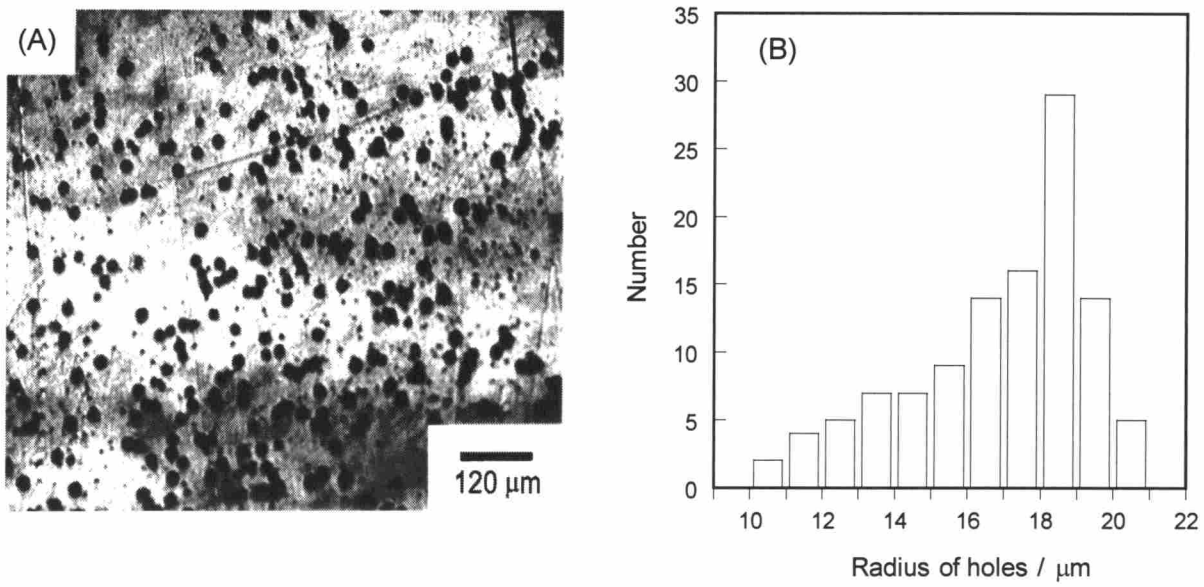

Figure 2.3

(A)Optical microscope image of the HDT/Au electrode having deposited copper. The electrode was immersed in 0.3 mol dm^{-3} KCN aqueous solution for 20 min before the electrodeposition of copper was made at - 0.5 V vs. Ag|AgCl for 10 s from 0.5 mol dm^{-3} $CuSO_4$. (B) Size-distributins of the depositted copper islands on the HDT/Au electrode.

2.3.3 Evaluation of Changes in Surface Coverage of Hexadecylthiolate on Au Electrode

Changes in the surface coverage of the adsorbed hexadecylthiolate during the course of immersion of the HDT/Au electrode in the KCN solution were evaluated by measuring the electrode capacitance and then by applying the capacitance to the equivalent circuit. The equivalent circuit used was assumed to be composed of the capacitance C_{dl} due to the electrical double-layer of the pinholes (i.e., microelectrodes) and C_m due to the remaining monolayer in parallel [22,23]. The value of C_m was determined to be 11 μF cm^{-2} by measuring the charging currents at -0.05 V vs. Ag|AgCl in cyclic voltammograms of the as-prepared HDT|Au electrode taken in 1 mol dm^{-3} KCl aqueous solution at the potential scan rate of 100 mV s^{-1}. In order to evaluate C_{dl} value, the capacitance of a naked Au electrode was measured in the same way as that mentioned above for the as-prepared HDT/Au electrode. Since microelectrodes in the HDT/Au were formed by reactions of cyanide ions with the gold electrode substrate, an Au electrode soaked in 0.3 mol dm^{-3} KCN aque-

ous solution for 5 min was used as the naked Au electrode. The value determined was 280 μF cm^{-2}. If the Au electrode was soaked in the same KCN solution for 70 min, 285 μF cm^{-2} was obtained as the capacitance value. Then, the capacitance of 280 μF cm^{-2} was used as C_{dl}. The electric capacitance of the HDT/Au electrode having pinholes (C_{exp}) is given by,

$$C_{exp} = \theta C_m + (1-\theta)C_{dl} \tag{2.2}$$

where θ is the surface coverage of the adsorbed hexadecylthiolate. Solving eq (2.2) with respect to θ yields

$$\theta = \frac{C_{exp} - C_{dl}}{C_m - C_{dl}} \tag{2.3}$$

Figure 2.4(A) shows the cyclic voltammograms of the HDT/Au electrodes prepared by soaking in 0.3 mol dm^{-3} KCN solution for 0, 10, 20, and 40 min. The charging and discharging currents increased with an increase in the soaking time of the electrode in the KCN solution. If the surface coverages estimated by the use of eq (2.3) are plotted as a function of the soaking time, a relationship as shown in Figure 2.4(B) is obtained. In this figure, results obtained by soaking in 0.1 and 0.2 mol dm^{-3} KCN solution are also given. It is clearly seen that the use of higher concentration of

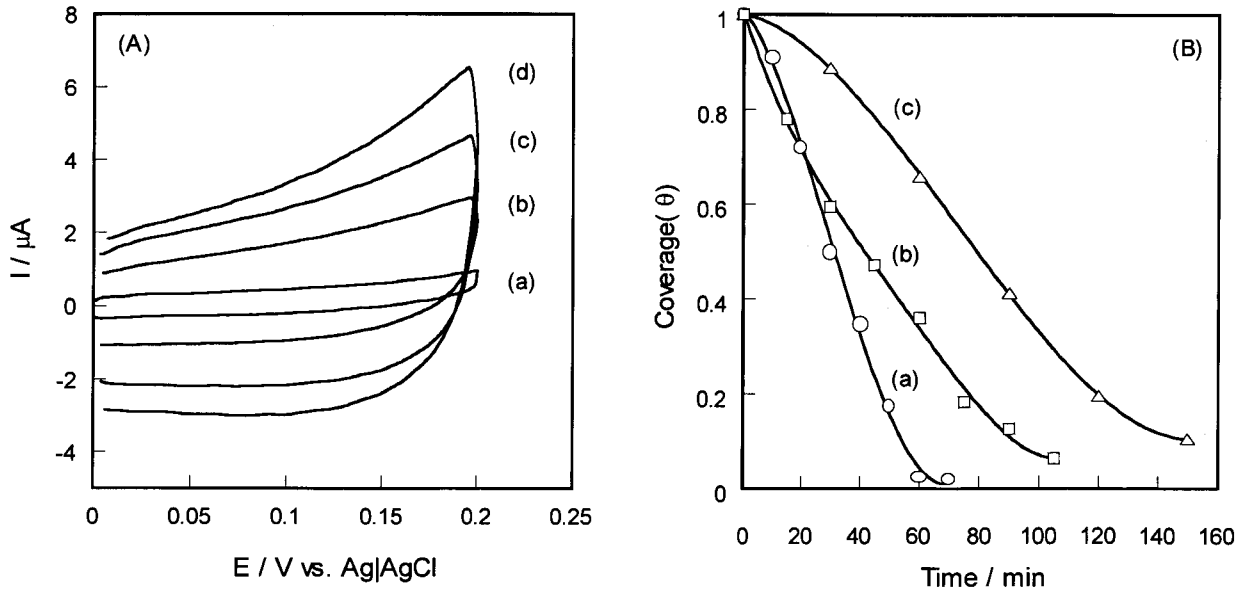

Figure 2.4

(A) Cyclic voltammograms taken in 1 mol dm^{-3} KCl aqueous solution at 100 mV s^{-1}. The measurements were taken after soaking the HDT/Au electrode in 0.3 mol dm^{-3} KCN aqueous solution for (a) 0 min, (b) 10 min, (c) 20 min and, (d) 40 min. (B) The surface coverage of hexadecylthiolate obtained using eq. (3). Soaking of the electrode in (a) 0.3 mol dm^{-3}, (b) 0.2 mol dm^{-3}, (c) 0.1 mol dm^{-3} KCN aqueous solution.

KCN caused more rapid desorption of the adsorbed thiolate. It is recognized that complete elimination of the SAM of hexadecylthiolate occurred with the soaking time in 0.3 mol dm^{-3} KCN solution for longer than 60 min. The coverage of the remaining SAM obtained at the soaking time of 20 min was 0.72 (i.e., the exposed area of 0.28) which accorded well with that obtained by the deposition of Cu on the same electrode (0.25) as described above.

2.3.4 Electrochemical Characterization of the KCN-treated HDT/Au Electrode

Theoretical studies on the microelectrodes array [24-28] gave the dimensionless currents ψ of cyclic voltammograms as given by eq (2.4)

$$\psi = I/[nFc^*(nFDv/RT)^{1/2}] \tag{2.4}$$

where I is the current density, c^* is the bulk concentration of redox active species, D is the diffusion coefficient of electroactive species, and v is the potential scan rate. ψ is also given as the solution of the following integral equation.

$$\psi = Ae^{\alpha\varepsilon}[(1-\mathbf{I}\psi - \psi/B) - (\mathbf{I}\psi + \psi/A)e^{-\varepsilon}] \tag{2.5}$$

where $\mathbf{I}\psi$ is the convolution integral of ψ given by eq (2.6), ε is dimensionless potential given by eq (2.7), and A and B are defined by eqs. (2.8) and (2.9).

$$\mathbf{I}\psi = \pi^{-1/2}\int_0^t \psi(t-\tau)d\tau \tag{2.6}$$

$$\varepsilon = -(nF/RT)(E-E^{o'}) \tag{2.7}$$

$$A = k^o(1-\theta)(RT/DFv)^{1/2} \tag{2.8}$$

$$B = (DRT(1-\theta)/Fv)^{1/2}/(0.6r_h) \tag{2.9}$$

The A and B are dimensionless parameters including the heterogeneous electron transfer rate constant (k^o), a half of the average distance between the centers of neighboring microelectrodes (r_h), and a ratio of inactive area (θ), and other parameters have their usual significance. Note that the radius of individual microelectrodes r_o is related to r_h and θ as given by [23],

$$r_o = r_h(1-\theta)^{1/2} \tag{2.10}$$

If literature values of diffusion coefficient (D = 6.8 x 10^{-6} cm^2s^{-1} [27]) and heterogeneous electron transfer rate constant (k^o = 0.0125 cm s^{-1} [27]) of $[Fe(CN)_6]^{3-/4-}$, and the values of θ which was estimated from the capacitance measurements (Figure 2.4) were used, the simulation of theoretically predicted cyclic voltammogram to the experimentally one can be made using r_h as a sole adjustable parameter. The numerical algorithm programed by Matsuda et al.[27] was used for the unfolding of eq (2.5) to obtain the theoretically expected current-voltage curve. Figures 2.5(A) and 2.5(B) shows the cyclic voltammograms of the HDT/Au electrodes in 50 mmol dm^{-3} $K_4[Fe(CN)_6]$ containing 1 mol dm^{-3} KCl after soaking the electrode in 0.3 mol dm^{-3} KCN solution for 20 and 30 min, respectively, and the best fitted simulation plots of the theoretically predicted voltammograms to them. Current values are given by the dimensionless current to compare the shape of voltammograms taken at different potential scan rate [27]. As shown in both Figures 2.5(A) and 2.5(B), good agreement is seen between the simulated voltammograms and the experimentally obtained ones, and in both cases the same r_h value of 33 μm was used to give the best fitted simulation curves while r_o values in those cases calculated using eq (2.10) were 18 and 23 μm for

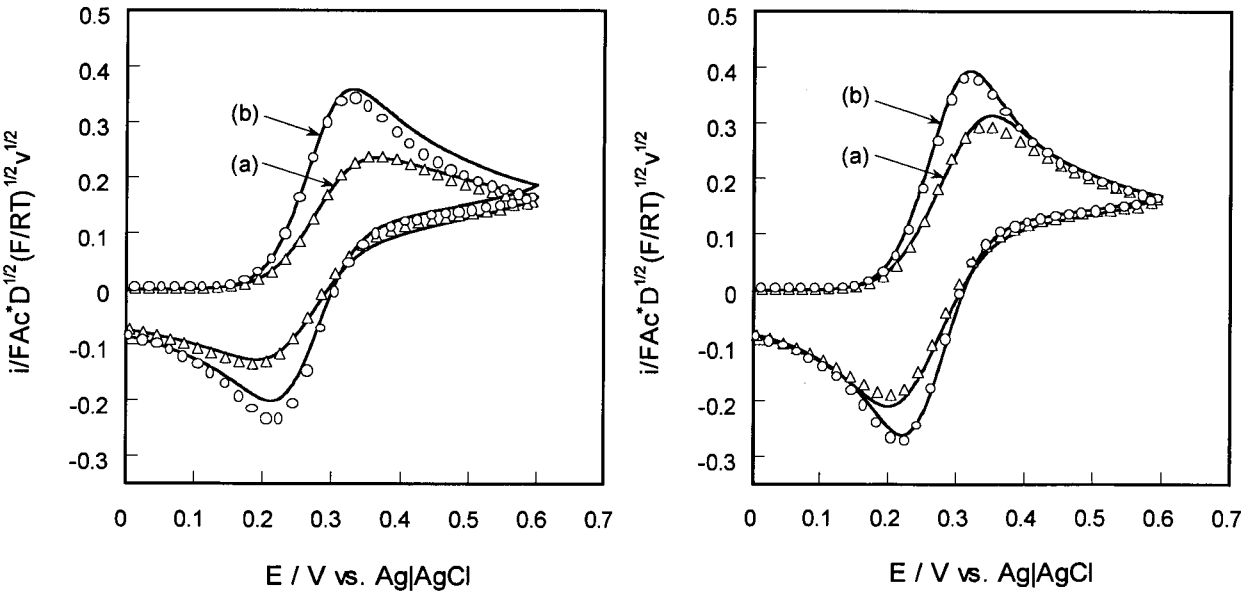

Figure 2.5

Cyclic voltammograms of the HDT/Au electrode taken in 1 mol dm^{-3} KCl aqueous solution containing 50 mmol dm^{-3} $K_4[Fe(CN)_6]$ at 50 (O) and 500 (Δ) mV s^{-1}, taken after soaking the HDT/Au electrode into 0.3 mol dm^{-3} KCN aqueous solution for (A) 20 and (B) 30 min, respectively. Solid curves are experimentally obtained cyclic voltammograms and plots of symbols are simulated ones using (A) r_h=33 μm, θ=0.72, and (B) r_h=33μm, θ=0.5 . Other parameters are shown in the text.

the 20 min and 30 min soaking, respectively. The r_o value of 18 μm estimated by simulation of the HDT/Au electrode prepared by soaking in the KCN solution for 20 min was in accordance with the average radius of microelectrodes obtained by observations of the Cu-deposition (17 μm), as shown in Figure 2.3. If the soaking of the HDT/Au electrode in the KCN solution was made for longer than 40 min, the shape of voltammograms was not changed by changing the potential scan rate, suggesting that the diffusion layers formed at individual microelectrodes were totally overlapped.

2.4 REFERENCES

1. A. Ulman, An Introduction to Ultrathin Organic Films, Academic Press, San Diego, 1991, Part Three, and the references cited in there.
2. A. Ulman, *Chemtech.*, (1995) 22.
3. A.J. Bard, H.D. Abruña, C.E. Chidsey, L.R. Faulkner, S.W. Feldberg, K. Itaya, M. Majda, O. Melroy, R.W. Murray, M.D. Porter, M.P. Soriaga, and H.S. Smith, *J. Phys. Chem.*, **97**(1993)7147.
4. E.Delamarche, B. Michel, H. Kang, and C. Gerber, *Langmuir*, **10**(1994)4103.
5. H.O. Finklea, S. Avery, and M. Lynch, and T. Furtsch, *Langmuir*, **3**(1987)409.
6. A.M. Becha, and C.J. Miller, *J.Phys. Chem.*, **96**(1992)2657.
7. C.B. Ross, L. Sun, and R.M. Crooks, *Langmuir*, **9**(1993)632.
8. N.L. Abbott, D.R.Rolison, and G.M. Whitesides, *Langmuir*, **10**(1994)2672.
9. C.R.K. Marrian, F.K. Perkins, S.L.Brandow, T.S. Koloski, E.A. Dobisz, and J.M. Calvert, *Appl. Phys. Lett.*, **64**(1994)390.
10. Y. Li, J. Huang, R. T. McIver, Jr and J. C. Hemminger, *J. Am. Chem. Soc.*, **114** (1992) 2428.
11. J. Huang and J. C. Hemminger, *J. Am. Chem. Soc.*, **115** (1993) 3342.
12. M. J. Tarlov, D. R. F. Burgess, Jr. and G. Gillen, *J. Am. Chem. Soc.*, **115** (1993) 5305.
13. J. Huang, D. A. Dahlgren and J. C. Hemminger, *Langmuir*, **10** (1994) 626.
14. K.C. Chan, T. Kim, J.K. Schoer, and R.M. Crooks, *J. Am. Chem. Soc.*, **117** (1995) 5875.
15. S.-W. Tam-Chang, H.A. Biebuyck , G.M. Whitesides, N.Jeon, and R.G. Nuzzo, *Langmuir*,

11(1995)4371

16. M. Lewis, M.Tarlov, and K. Carron, *J.Am.Chem.Soc.*, **117**(1995)9574.
17. M. Ohtani, T. Sunagawa, and S. Kuwabata, and H. Yoneyama, *J. Electroanal. Chem.*, **396** (1995) 97.
18. T. Ohno, Analyst, **114** (1989) 854.
19. W.G. McGlimpsey and J.C. Scaiano, *J.Am.Chem.Soc.*, **111**(1989)335.
20. A. Kumar , H.A. Biebuyck, N.L. Abbott, and G.M. Whitesides, *J.Am.Chem. Soc.*, **114**(1992)9188.
21. Y. Xia, X.-M. Zhao, E. Kim, and G.M. Whitesides, *Chem.Mater.*, **7**(1995)2332.
22. E. Sabatani and I. Rubinstein, *J. Phys. Chem.* **91** (1987) 6663.
23. E. Sabatani, I. Rubinstein, R. Maoz, and J. Sagiv, *J. Electroanal. Chem.*, **219** (1987) 365.
24. C. Amatore, Physical Electrochemistry, I. Rubinstein Ed., Marcel Dekker, New York, 1995, Chapter 4, and the references cited in there.
25. C. Amatore, J.M. Saveant, and D. Tessier, *J. Electroanal. Chem.*, **147** (1983) 39.
26. T. Gueshi, K. Tokuda, and H. Matsuda, *J. Electroanal. Chem.*, **89** (1978) 247.
27. T. Gueshi, K. Tokuda, and H. Matsuda, *J. Electroanal. Chem.*, **101** (1979) 29.
28. J. Cassidy, J. Ghoroghchaian, F. Sarfarazi, J. J. Smith, and S. Pons, *Electrochim. Acta*, **31** (1986) 629.

chapter 3

Electrochemical Oxidation of Reduced Nicotinamide Coenzymes at Au Electrode Modified with Phenothiazine Derivatives Monolayer

3.1 INTRODUCTION

The oxidation of β-nicotinamideadenine dinucleotide (NADH) to its oxidized form (NAD^+) has attracted much interest from the viewpoint of the high utility of the reaction in biosensors and bioreactors where NAD^+-dependent dehydrogenases are usually used [1]. NADH can be oxidized electrochemically at conventional electrodes such as Pt and Au, but in these cases high overpotentials of about 1 V are required due to a very low reaction rate of the oxidation [2,3], and then it is desired to find out efficient electrocatalysts for NADH oxidation. It has been reported that several kinds of quinone derivatives [4-9] and redox dyes such as phenoxazine and phenothiazine derivatives [10-15] possess catalytic activities for the oxidation of NADH. The investigations have been mostly carried out by immobilizing these substances on the electrode surface by various means; physical adsorption onto carbon electrodes [4-6, 10-12], covalent binding to an oxidized carbon electrode surface [4], adsorption of polymers derivatized with *o*-quinone moieties onto carbon electrodes [7, 8], electrodeposition of quinone derivatives on carbon electrodes [9], and electrochemical polymerization of phenothiazine derivatives on carbon electrodes [13, 14, 15].

Recently, a self-assembled monolayer [16] of thiol or disulfide on Au electrodes has been utilized to attach special functions to the electrodes with a high density [17-31]. Beside direct attachments of electrochemically active thiol or disulfide to the electrode [17, 18], binding of electrochemically active substances to electrochemically inert thiol or disulfide monolayer on Au has also been attempted [19-28]. Among a variety of studies in this area, electrocatalytic elec-

trodes for oxidation of NADH have been prepared by covalently binding pyrroloquinolinequinone (PQQ) to a self-assembled monolayer of cystamine on an Au electrode [27, 28] and several kinds of phenothiazine and phenoxazine derivatives to a self-assembled monolayers of mercaptopropionate [29], cystamine and cysteine [30] on an Au electrode. These studies demonstrated definitely the utility of self-assembled monolayers in designing electrocatalytic electrodes, but kinetic studies in systematic ways have not yet been made to clarify effects of the immobilized redox species on their catalytic activities.

This chapter describes kinetic studies on electrocatalytic oxidation of NADH on an Au electrode coated with a monolayer of phenothiazine derivatives such as thionine, azure C, and azure A. The electrode substrate was previously coated with a monolayer of 3,3'-dithiobis(succineimidylpropionate) [31] and the above phenothiazine derivatives were covalently bound to the monolayer. It will be shown that the prepared electrodes possess high catalytic activity for the oxidation of NADH, and the discussion focuses on the determination of the second-order reaction rate constant between NADH and monomer and dimer species immobilized on the electrode.

3.2 EXPERIMENTAL SECTION

All chemicals used in this study were of reagent grade and used without further purification. Water was purified by twice distillation of deionized water. An Au wire of 0.4 mm diameter was used as the electrode substrate, and was encapsulated in a glass tube using an insulating wax, Daifloil® (Daikin Co., Ltd.) except for the electrode area of 0.25 cm^2. Before use the electrode was stored in concentrated H_2SO_4, and just prior to use it was immersed in concentrated HNO_3 for 15 min, followed by rinsing with distilled water.

The immobilization of phenothiazine derivatives in an oxidized state on the Au electrode was accomplished using the reaction scheme shown in Scheme 2.1, which was developed by Katz [31]. A self-assembled monolayer of 3,3'-dithiobis(succineimidylpropionate) (DSP, Nacalai) was prepared by soaking overnight the Au electrode in dimethylsulfoxide (DMSO) containing 10 mmol dm^{-3} DSP, followed by being rinsed with 0.1 mol dm^{-3} phosphate buffer (pH 7.0). The electrode

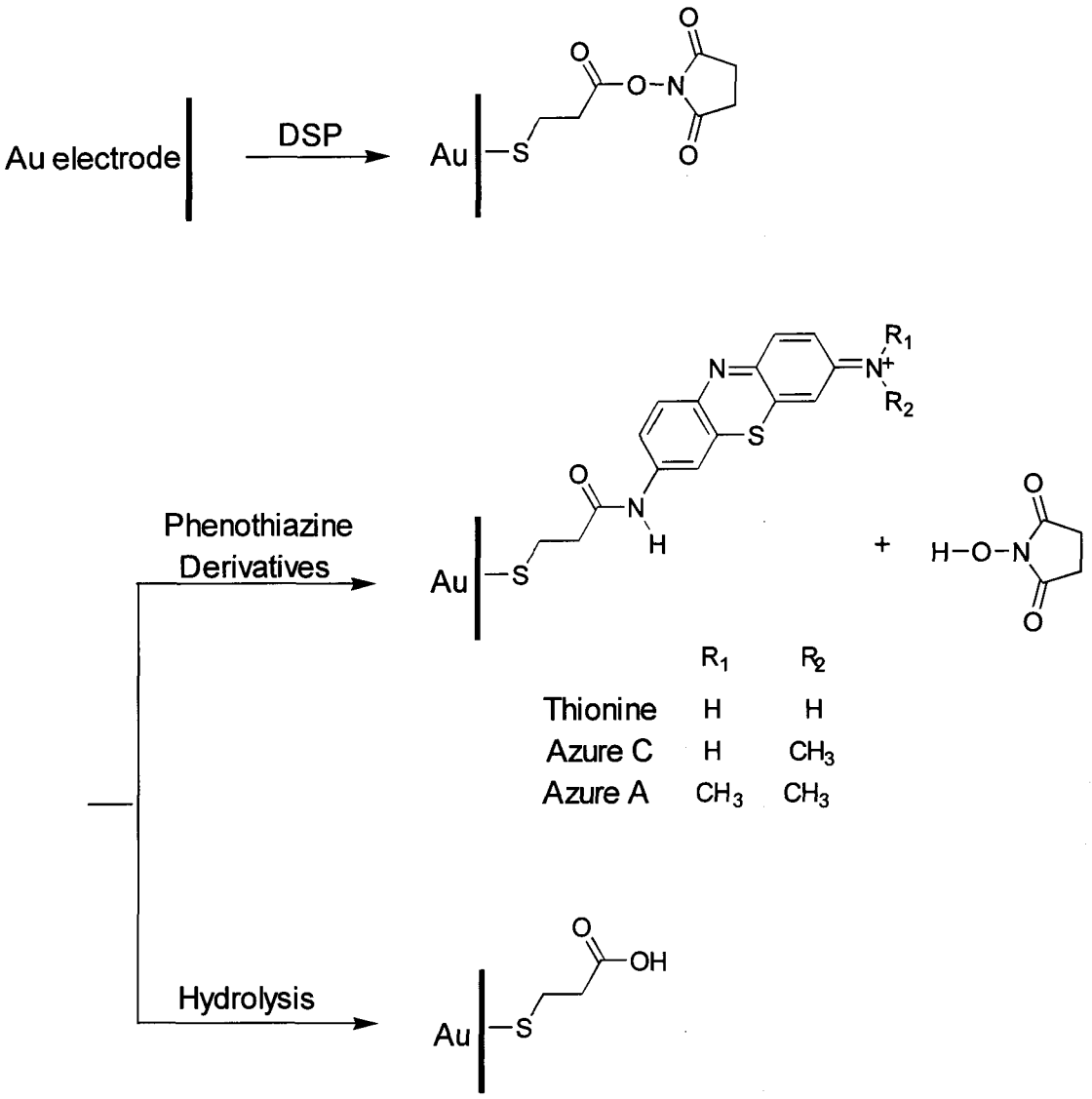

Scheme 3.1

Illustration of chemical modification procedure.

was then immersed in a phosphate buffer solution containing one of the phenothiazine derivatives (thionine (Aldrich), azure A (Nacalai), or azure C (Nacalai)) of 0.1 mmol dm^{-3} for more than 4 h to bind it covalently to the DSP monolayer. The phenothiazine derivatives which were adsorbed on the electrode without making covalent bonds were removed by polarization of the electrodes at -400 mV vs. Ag|AgCl in 0.1 mol dm^{-3} phosphate buffer (pH 7.0) under vigorous stirring for a few minutes. The Au electrode coated with a monolayer of thionine, azure A, and azure C will be denoted here as Th/Au, AzA/Au, and AzC/Au, respectively. When the immobilization of reduced thionine was attempted, the Au electrode coated with DSP monolayer was polarized at -400 mV vs. Ag|AgCl for 4 h in 0.1 mol dm^{-3} phosphate buffer containing 0.1 mmol dm^{-3} thionine. The

resulting electrode will be denoted as Th(r)/Au to distinguish it from the Th/Au electrode prepared without polarization of the electrode. All the modifications of the electrode were carried out under thermostated conditions at 25 ± 1 °C.

Electrochemical measurements were carried out under thermostated conditions at 25 ± 1 °C using a BAS100-B/W electrochemical analyzer connected to a Gateway 2000 computer. An Ag|AgCl|KCl (saturated) electrode and a Pt foil were used as a reference and a counter electrode, respectively. N_2 gas was thoroughly bubbled into the electrolyte solution prior to measurements. In cases of cyclic voltammetry using high potential sweep rates, *IR* drop due to solution resistance was electronically compensated by an automatic *IR* compensator equipped to BAS 100-B/W.

The catalytic activities of the oxidized form of thionine, azure A, and azure C for chemical oxidation of NADH (Oriental Yeast Co., Ltd.) were investigated by measuring changes in absorbance at 600 nm using a Hewlett-Packerd 8452A diode array spectrophotometer. For this purpose 0.1 mmol dm^{-3} dye solution and 0.1 mmol dm^{-3} NADH solution were prepared using 0.1 mol dm^{-3} phosphate buffer (pH 7.0), and were deaerated by bubbling with N_2 gas for 15 min. After mixing both solutions of 0.75 mL each, the absorbance change was monitored.

3.3 RESULTS AND DISCUSSION

3.3.1 Oxidation of NADH by Phenothiazine Derivatives in Homogeneous System

Rates of chemical oxidation of NADH to NAD^+ by the oxidized form of thionine, azure A, and azure C were evaluated from changes in absorbance at 600 nm where the oxidized form of these substances shows intense absorption but their reduced form does not. The changes in absorbance obtained are shown in Figure 3.1. The chemical oxidation reaction of NADH is represented by

$$P^+ + NADH \rightarrow PH + NAD^+ \qquad (3.1)$$

where P^+ and PH denote, respectively, the oxidized form and the reduced form of phenothiazine

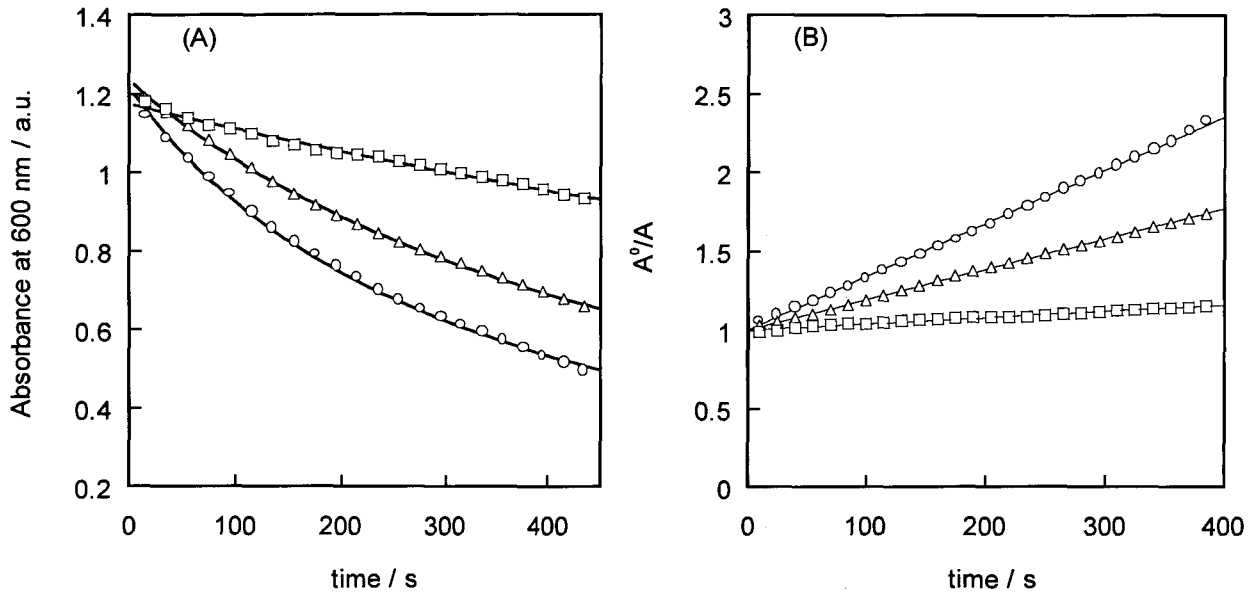

Figure 3.1

(A) Time course of absorbance changes at 600 nm of 0.1 mol dm^{-3} phosphate buffer (pH 7.0) containing 50 μmol dm^{-3} NADH and one of thionine (○), azure C (△), or azure A (□) in 50 μmol dm^{-3}. (B) Changes in a relative absorbance $A°/A$ with the reaction time obtained from the results shown in (A), where $A°$ and A are absorbance at time $t = 0$ and at t, respectively.

derivatives. The reaction rate for reaction (3.1) is given by

$$-\frac{d[P^+]}{dt} = k_h[P^+][NADH] \tag{3.2}$$

where k_h is the second-order reaction rate constant. As mentioned in the experimental section, P^+ and NADH were dissolved in the same concentration. If the initial concentration and the concentration at time t of P^+ are given by $c°$ and c, respectively, eq (3.3) holds

$$c°/c = k_h c°t + 1 \tag{3.3}$$

According to the Lambert-Beer's law, the term of $c°/c$ is equivalent to $A°/A$ where $A°$ and A are the absorbance of the dye solution obtained before oxidation of NADH and that obtained at the reaction time t. Since the plots of $A°/A$ as a function of the reaction time gave a linear relationship with the correlation coefficients greater than 0.997 as shown in Figure 3.1 (B), k_h was evaluated with a

fairly high precision, and 64.2, 39.8, and 11.8 mol^{-1} dm^3 s^{-1} were obtained for thionine, azure C, and azure A, respectively.

The redox potential of thionine, azure C, and azure A were determined to be -120 mV, -135 mV, and -165 mV vs. Ag|AgCl in 0.1 mol dm^{-3} phosphate buffer, respectively, by means of cyclic voltammetry using a glassy carbon electrode. Using these redox potential values together with the reported redox potential of NADH of -540 mV vs. Ag|AgCl [32], the Gibbs energy changes (ΔG^o) of oxidation of NADH with thionine, azure C, and azure A in 0.1 mol dm^{-3} phosphate buffer at pH 7 were estimated to be -81.1, -78.2, and -72.3 kJ mol^{-1}, respectively. If logarithms of k_h values obtained above are plotted as a function of the corresponding ΔG^o, a good linear relationship is obtained between the two, indicating that these electron-transfer reactions are controlled by ΔG^o.

3.3.2 Preparation of Phenothiazine Derivatives-immobilized Au Electrode and Their Electrochemical Responses

The immobilization of phenothiazine derivatives on an Au electrode was made by the reaction scheme given in Scheme 3.1 in which acylation reaction of amino groups of phenothiazine derivatives is essential for making covalent bonds with the DSP monolayer. The feasibility of the acylation reaction using succineimide active ester was confirmed by synthesis of acyl derivatives of azure A. N-succinimidylpropionate (Wako) was added to an aqueous solution containing 10 mmol dm^{-3} azure A so as to give the final concentration of 10 equivalents and the solution was stirred for 5 h. The resulting dye molecules were collected by adsorbing on silica-gel, followed by washing successively the dye-adsorbed silica-gel with copious water and methanol. The dye molecules were desorbed by dispersing the silica-gel in methanol containing 2 vol.% HCl and were dried in vacuum. Comparison of FT-IR spectrum of the final product to that of azure A revealed the appearance of new adsorption bands at 1650, 2850, and 2915 cm^{-1}. The band at 1650 cm^{-1} was assignable to the characteristic adsorption of C=O in amide group and the bands at 2850 and 2915 cm^{-1} were due to C-H stretching of alkyl group, indicating that the acylation reaction took place with just mixing N-succinimidylpropionate and azure A. Then it was definitely expected that phenothiazine derivatives were covalently bound to the DSP monolayer by acylation reaction, as

given by Scheme 3.1. The Au electrode having immobilized phenothiazine derivatives possessed redox activities due to the redox dyes, as will be shown below.

Figure 3.2 shows cyclic voltammograms of the Th/Au electrode taken in 0.1 mol dm^{-3} phosphate buffer (pH 7.0) in a potential range between -300 and +450 mV vs. Ag|AgCl. The voltammogram (a) was obtained at an as-prepared Th/Au electrode which was not subjected to any reductive polarization. In that case, three redox waves appeared, whose average potentials of anodic and cathodic peaks were -170, -30 and +240 mV vs. Ag|AgCl. Similar redox behavior giving three redox waves was reported for an Au electrode coated with a self assembled monolayer of 3-mercaptopropionate to which toluidine blue O (TOB) was chemically bound [29]. However, if the Th/Au electrode was polarized under vigorous agitation of the electrolyte solution at -400 mV vs. Ag|AgCl, which was negative enough to reduce the adsorbed thionine, the redox wave observed at -170 mV disappeared, as shown by voltammogram (b) of Figure 3.2, indicating that this redox wave was due to adsorbed thionine molecules which were not covalently bound to the self-assembled monolayer. The presence of such adsorbed thionine molecules on the Th/Au electrode must be due to the positive charges on the thionine molecules which allow electrostatic binding to the negatively charged propionate groups generated by hydrolysis of DSP on Au [33]. It was also suggested that formation of dimeric thionine due to the London force (i.e., π-electron stacking) took place between the chemically bound thionine on the gold substrate and dissolved molecule in the oxidized state [34]. Thionine molecules physically adsorbed due to electrostatic interaction and the London force must be desorbed by negative polarization because neither electrostatic interaction nor the London force operate at the reduced thionine molecule [34]. Therefore, the remaining redox waves after the nega-

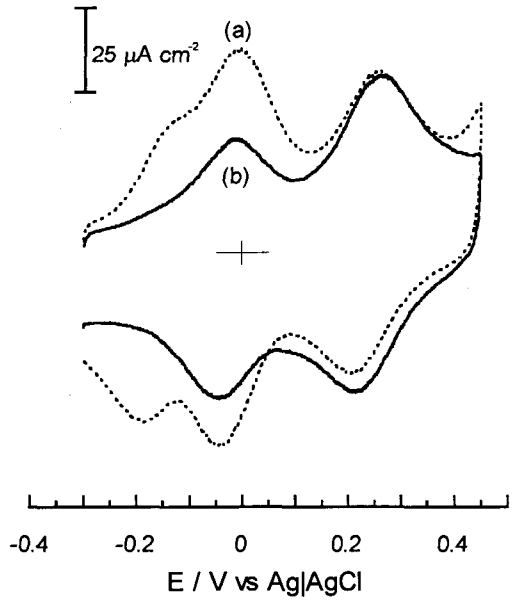

Figure 3.2

Cyclic voltammograms of the Th/Au electrode taken in 0.1 mol dm^{-3} phosphate buffer (pH 7.0) at the potential scan rate of 200 mV s^{-1} before (a, - - - -) and after (b, —) polarization at -400 mV vs. Ag|AgCl under agitation of electrolyte solution.

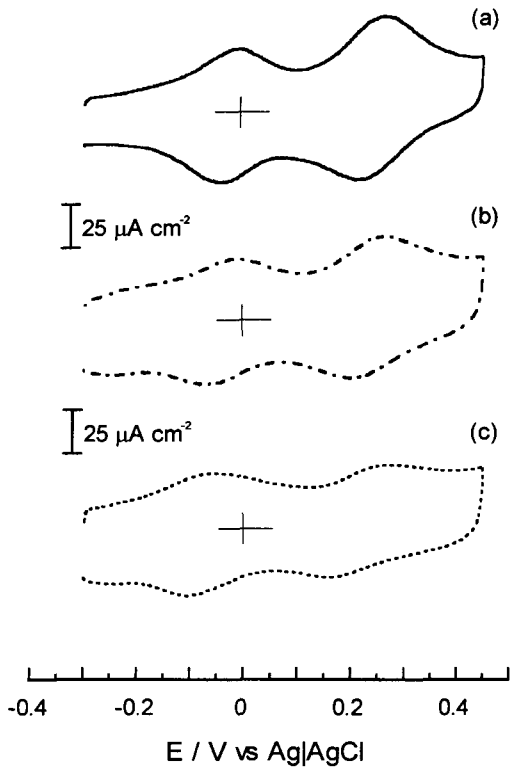

Figure 3.3

Cyclic voltammograms of (a) the Th/Au (—), (b) the AzC/Au (— - —), and (c) the AzA/Au (- - - -) electrodes taken in 0.1 mol dm^{-3} phosphate buffer (pH 7.0) at potential sweep rate of 200 mV s^{-1} after polarization at - 400 mV vs. Ag|AgCl for a few minutes.

tive polarization should be ascribed to thionine covalently immobilized to the DSP-monolayer thorough amide bonding. Why the chemically bound thionine showed two redox waves will be discussed below. The electrochemical responses giving three couples of redox reactions as observed at the as-prepared Th/Au electrode were also observed at the as-prepared AzA/Au and AzC/Au electrodes. If polarization of these electrodes was made at -400 mV vs. Ag|AgCl, the redox wave at the most negative potential was eliminated as Figure 3.3 shows.

The redox wave at -30 mV vs. Ag|AgCl of the Th/Au electrode can be ascribed to thionine monomers covalently immobilized on the electrode surface through amide bonding. Its redox potential was 90 mV more positive than the original redox potential of thionine dissolved in the electrolyte solution. This positive shift of the redox potential seems reasonable because the electron-withdrawing property is enhanced by the transformation of the amino group in position 3 of the phenothiazine derivatives into the amide group [35]. Schlereth et al. reported that a dimer species formed at the TOB monolayer-coated Au electrode gave the most positive redox potential among three redox waves observed [29]. The same might be true for the electrochemical responses observed at the Th/Au electrode. In order to confirm this assumption, the immobilization of thionine onto the DSP monolayer-coated Au electrode was performed under polarization of the electrode at -400 mV vs. Ag|AgCl. The cyclic voltammogram of the resulting electrode (Th(r)/Au) is shown in Figure 3.4 together with that obtained for the Th/Au which was given by curve (b) in Figure 3.2. The Th(r)/Au electrode exhibited a pair of anodic and cathodic waves only. The

similar changes in the voltammetric behavior caused by polarization of the electrode during the course of immobilization was reported for the above mentioned TOB monolayer-coated Au electrode [29, 30]. The average potential of anodic and cathodic peaks at the Th(r)/Au electrode was -45 mV vs. Ag|AgCl which was close to the formal potential of a thionine monomer observed at the Th/Au electrode. However, the redox waves observed around 240 mV in the voltammogram of Th/Au is not seen at Th(r)/Au. As mentioned above, thionine molecules in oxidized state give easily its dimeric species because they have a high equilibrium constant (K_d=[dimer]/[monomer]^2>10^3) due to the London forces, whereas their reduced form is not [34]. Accordingly, if the immobilization was carried out without any polarization, dimers would be predominantly immobilized. If only one thionine molecule of dimer is covalently immobilized through amide bonding, another thionine molecule of the dimer must be eliminated by negative polarization as mentioned above, leaving the immobilized monomer. If this is the case, the subsequent positive potential scan will not result in any significant wave characteristics of the dimer which is discussed below. Since the two pairs of redox waves appeared even after the negative polarization, two thionine molecules of the dimer must be covalently immobilized through amide bonding to the DSP-monolayer on Au electrode. If the immobilized dimer is reduced, two monomers are formed which are believed to possess a favorable geometric arrangement for re-dimerization to take place with subsequent oxidation, while an immobilized monomer would not be dimerized due to limitation of its motion on the electrode surface and the absence of the partner for dimerization to take place. Such differences in the immobilized states between the monomer and dimer of thionine would result in difference in the apparent redox potentials, though we cannot present any quantitative discussion on the magnitude of the redox potential difference because the voltammetric behavior of surface-con-

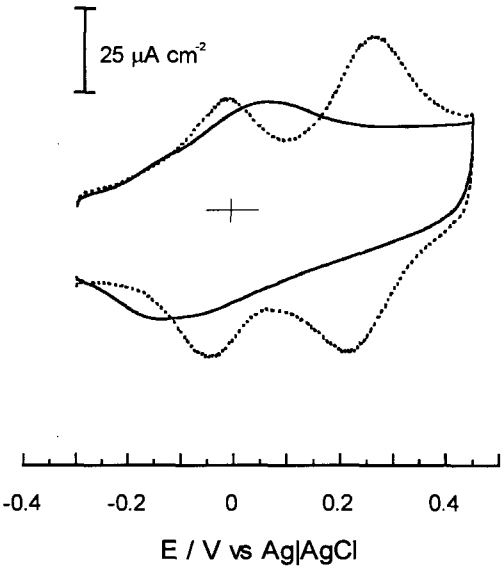

Figure 3.4

Cyclic voltammograms of the Th(r)/Au (—) and the Th/Au electrode (- - -) taken in 0.1 mol dm^{-3} phosphate buffer (pH 7.0) at 200 mV s^{-1}.

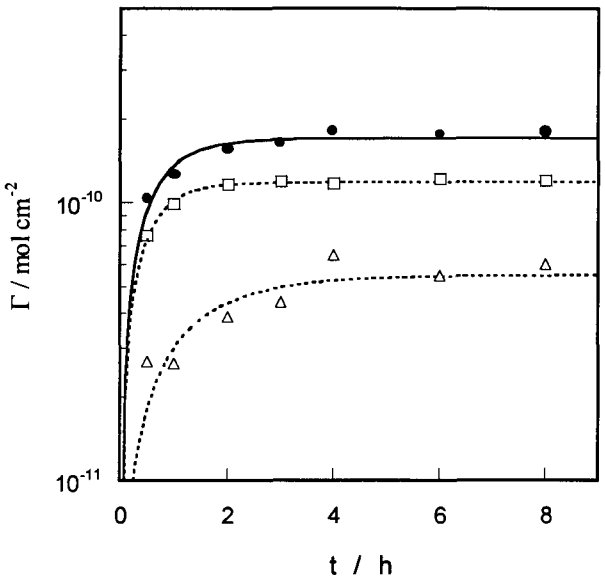

Figure 3.5

Changes in surface coverage of thionine in monomeric (□), dimeric states (△), and both of them (●) immobilized on Au electrode as a function of immersion time of DSP-coated Au electrode in 0.1 mmol dm^{-3} thionine solution.

fined redox species must be affected by their degree of solvation and dielectric constant [36], but no established technique to predict the redox potentials including these factors is available. It is evident that dissolved thionine in homogeneous media gives one pair of redox waves only, because the monomers and the dimers in oxidized state are in equilibrium. If the electrode is negatively polarized during the course of the immobilization, the monomer alone must be immobilized. Then, it seems reasonable to assign the redox wave at 240 mV in the voltammogram of Th/Au electrode to the redox reaction of the immobilized thionine dimer. The same discussion might be true for the AzA/Au and the AzC/Au electrode. Hereafter, the two pairs of redox waves will be distinguished each other by the term of monomer and dimer.

The amount of surface coverage of the immobilized thionine was evaluated by integrating the anodic peak area under an assumption that two electrons were involved in the redox reaction of one thionine molecule. Figure 3.5 shows the surface coverage of monomeric and dimeric thionine, and the sum of them as a function of immersion time of the DSP-coated Au electrode in the thionine solution. As shown in this figure, the surface coverage of thionine monomer was saturated at 5.8 x 10^{-11} mol cm^{-2} with the electrode immersion time of 4 h, whereas that of thionine dimer was saturated to as high as 1.2 x 10^{-10} mol cm^{-2} with the immersion time of 2 h, giving the total surface coverage of adsorbed thionine of 1.78 x 10^{-10} mol cm^{-2}. As for the AzC/Au and AzA/Au electrodes, the total amounts of adsorbed molecules were 1.1 x 10^{-10} and 0.9 x 10^{-10} mol cm^{-2}, respectively.

If cyclic voltammograms of the Th/Au electrode prepared without polarization were taken in 0.1 mol dm^{-3} phosphate buffer (pH 7.0) at several different potential sweep rates ranging from 20 to

500 mV s^{-1}, the peak currents of the redox waves of both monomer and dimer increased in proportion to the potential sweep rate, indicating that the immobilized thionine exhibited electrochemical responses characteristic of the redox species confined on the electrode. Figure 3.6 shows the magnitude of separation of the peak potentials between the anodic and cathodic waves of the two redox couples as a function of the potential sweep rate. Application of Laviron's method [37] to the results shown in Figure 3.6 gave the electron transfer rate constant of ca. 50 s^{-1} for the immobilized thionine. In this evaluation, the transfer coefficient was assumed to be $\alpha = 0.5$ because the dependence of the cathodic peak potentials on logarithm of the potential scan rate was nearly equal to that of the anodic peak potential in absolute value. Similar results were obtained for the AzC/Au (ca. 50 s^{-1}) and the AzA/Au (ca. 45 s^{-1}) electrode. The electron transfer rates obtained here are large enough to give the Nernstian voltammetric behavior of the immobilized species if measurements are made at potential sweep rates less than several hundreds mV s^{-1} [38].

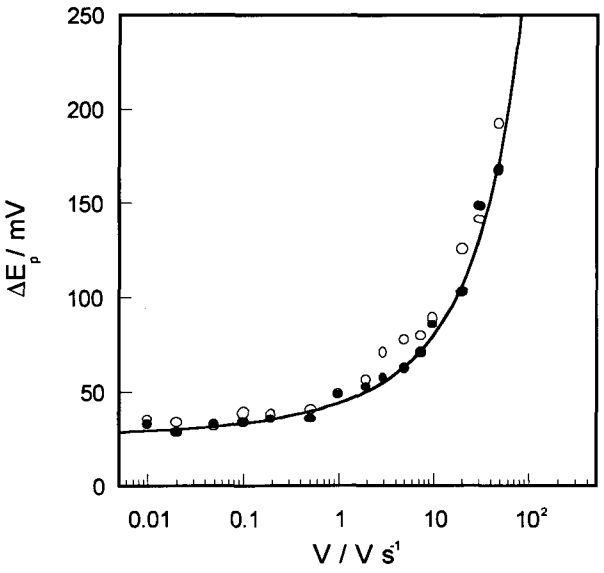

Figure 3.6

Plots of the peak separation (ΔE_p) of redox couples due to monomer (●) and dimer (○) species of the Th/Au electrode taken in 0.1 mol dm^{-3} phosphate buffer (pH 7.0) as a function of potential sweep rate.

3.3.3 Electrochemical Oxidation of NADH

Cyclic voltammograms of the Th/Au electrode taken in the phosphate buffer (pH 7.0) in the presence and absence of 1 mmol dm^{-3} NADH are shown in Figure 3.7. When the electrolyte solution contained NADH, an irreversible anodic wave appeared in potentials positive of the redox wave of the thionine monomer immobilized on the electrode. If the same experiment was conducted using a bare Au electrode, no anodic wave appeared in the same potential range, indicating that thionine molecules immobilized on the Au electrode worked well as an electrocatalyst for

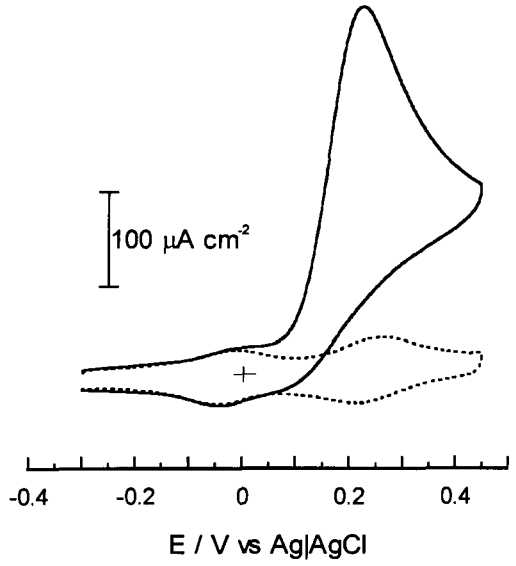

Figure 3.7

Cyclic voltammograms of the Th/Au electrode taken in 0.1 mol dm^{-3} phosphate buffer (pH 7.0) in the presence (—) and absence (- - - -) of 1 mmol dm^{-3} NADH at 200 mV s^{-1}.

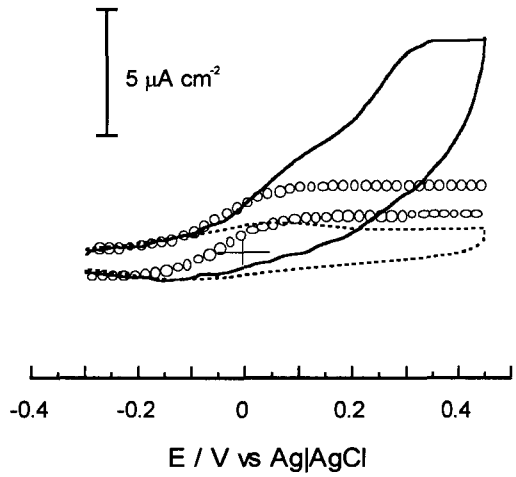

Figure 3.8

Experimentally obtained cyclic voltammograms of the Th(r)/Au electrode taken in the presence (—) and absence (– - - -) of 1 mmol dm^{-3} NADH at 200 mV s^{-1} and simulated ones (○). Parameters used in the simulation are given in the text.

oxidation of NADH. If the potential sweep was repeated, a gradual decrease in the anodic peak currents was noticed, but the voltammogram shown in Figure 3.7 was recovered by polarizing the electrode for a few minutes at the lower potential limit of -300 mV vs. Ag|AgCl chosen in the cyclic voltammetry without changing the solution, suggesting that the observed current decrease resulted from a decrease in the concentration of NADH on the electrode surface due to its consumption and/or adsorption of some impurities arising from NADH oxidation [12] rather than due to desorption of thionine from the electrode. The peak currents of the voltammograms were proportional to square root of the potential sweep rate from 10 to 100 mV s^{-1} if the bulk concentration of NADH was below 2 mmol dm^{-3}, suggesting that diffusion of NADH predominated in the oxidation processes of NADH, which occured with EC mechanism at the Th/Au electrode [39].

Figure 3.8 shows cyclic voltammograms of the Th(r)/Au electrode taken under the same conditions as those given in Figure 3.7. The increase in the oxidation currents was observed at potentials positive of -120 mV vs. Ag|AgCl where oxidation of the immobilized thionine took place. However, the catalytic currents obtained were very small compared to those obtained at the Th/

Au electrode, giving no definite peak currents in the potential range chosen for the measurements. The results show clearly that the dimeric form of thionine has much higher catalytic activity for oxidation of NADH. In this figure, simulation plots for the catalytic oxidation of NADH are also shown by open circles. The procedures of obtaining simulation curves will be described in the next section.

The AzC/Au and the AzA/Au electrodes prepared without any polarization also exhibited high catalytic activities for oxidation of NADH, but the peak currents obtained at these electrodes were a little smaller than that obtained for the Th/Au electrode (see Figure 3.9).

3.3.4 Kinetic Studies on Electrocatalytic Oxidation of NADH

As already shown in Figure 3.7, the thionine molecules immobilized on the Au electrode substrate worked well as an electrocatalyst for electrochemical oxidation of NADH. However, since only one wave appeared in the oxidation of NADH, it is difficult to distinguish whether the monomeric or dimeric species immobilized on the electrode contributed to the catalytic oxidation of NADH. The same was true for electrochemical measurements using a rotating disk electrode (RDE) technique, where a catalytic current having a simple sigmoidal shape was obtained, suggesting that one kind of redox species efficiently worked as the electrocatalyst. Then, digital simulations using an explicit finite difference calculation [38, 40] were used to evaluate the rate constant of the electron exchange between NADH and each immobilized species. The technique used here was based on the work developed recently by Xie and Anson [38]. Though the preceding works on theoretical treatments of cyclic voltammetry for surface-confined electrocatalysis [39, 41] was available, whole current-voltage curves obtained by using them did not give good fit to the experiment.

If both monomeric and dimeric species of phenothiazine derivatives immobilized on the electrode are taken into consideration in the catalytic oxidation of NADH, the oxidation reactions are given by

$$M_{red,1} \rightleftharpoons M_{ox,1} + 2e^- + H^+ \quad \text{(formal potential: } E_1^{o'}\text{)} \tag{3.4.a}$$

$$M_{red,2} \rightleftharpoons M_{ox,2} + 2e^- + H^+ \quad \text{(formal potential: } E_2^{o'}\text{)} \tag{3.4.b}$$

$$M_{ox,1} + NADH \xrightarrow{k_{c,1}} M_{red,1} + NAD^+ \quad (3.5.a)$$

$$M_{ox,2} + NADH \xrightarrow{k_{c,2}} M_{red,2} + NAD^+ \quad (3.5.b)$$

where $M_{ox,i}$ and $M_{red,i}$ (i = 1, 2) denote the immobilized phenothiazine derivatives in the oxidized and reduced form, respectively, $k_{c,i}$ is the second-order reaction rate constant of the catalytic chemical reaction, and the subindex 1 and 2 denote the surface-bound phenothiazine derivatives in monomeric and dimeric states, respectively. Since both monomeric and dimeric species exhibited the Nernstian redox behavior as mentioned above, the modified Nernst equation [38] as given by eq.(3.6) is useful to correlate the electrode potential and the surface coverage of the immobilized species of oxidized ($\Gamma_{ox,i}$) and reduced ($\Gamma_{red,i}$) forms.

$$E = E_i^{o'} + \frac{RT}{nFg_i} \ln\left(\frac{\Gamma_{ox,i}}{\Gamma_{red,i}}\right) \quad (3.6)$$

where g_i is an empirical parameter that is valid for expressing an non-idealized voltammetric behavior of the redox species immobilized on an electrode and its value is estimated from a full-width at half-maximum (FWHM) of the cathodic or anodic wave, i.e., FWHM = $90.6/(ng_i)$ mV [38]. The n value is the number of electrons involved in the redox reaction, and F, R, and T have their usual significance. The sum of $\Gamma_{ox,i}$ and $\Gamma_{red,i}$ is given here by Γ_i.

$$\Gamma_i = \Gamma_{ox,i} + \Gamma_{red,i} \quad (3.7)$$

The current density at the time of t after initiating the potential sweep ($j(t)$) is composed of that of the redox reactions of the immobilized phenothiazine derivatives ($j_0(t)$), that of charging and discharging of the double layer (j_c), and that of the catalytic oxidation of NADH ($j_{cat}(t)$).

$$j(t) = j_0(t) + j_{cat}(t) + j_c \quad (3.8)$$

The $j_0(t)$ can be obtained by

$$j_0(t) = nF\frac{d\Gamma_{ox,i}(t)}{dt} = -nF\frac{d\Gamma_{red,i}(t)}{dt} \tag{3.9}$$

where $\Gamma_{ox,i}(t)$ and $\Gamma_{red,i}(t)$ are the surface coverage of the immobilized species of oxidized and reduced forms at time t, respectively. By substituting eqs (3.6) and (3.7) into eq (3.9), eq (3.10) is obtained.

$$j_0(t) = \sum_{i=1}^{2} \frac{4F^2 v g_i \Gamma_i \exp\left[\frac{2Fg_i}{RT}\left(E(t) - E_i^{o'}\right)\right]}{RT\left\{1+\exp\left[\frac{2Fg_i}{RT}\left(E(t) - E_i^{o'}\right)\right]\right\}^2} \tag{3.10}$$

where v is the potential sweep rate, and positive values hold for positive potential scan, and $E(t)$ is the electrode potential at time t.

The charging currents of the double layer j_c is assumed to be independent of $E(t)$ and is given by the product of the double layer capacity (C_d) and the potential sweep rate v.

$$J_c = C_d v \tag{3.11}$$

If it is assumed that current values at -0.25 V vs. Ag|AgCl of cyclic voltammograms taken in the NADH-free electrolyte solution give the double layer charging currents, 60 μF cm^{-2} is obtained for C_d, which was used for all digital simulations of cyclic voltammograms. The j_c value may contain some error, but even if it is the case, the contribution of j_c to the total electrolysis current is very small as compared to the contribution of the catalytic current, resulting in no serious errors in the following discussion.

The anodic current due to oxidation of NADH catalyzed by the immobilized phenothiazine derivatives is given by

$$j_{cat}(t) = 2Fc_{NADH}(r_0, t)\sum_{i=1}^{2} k_{c,i}\Gamma_{ox,i}(t) \tag{3.12}$$

where $c_{NADH}(r_0,t)$ is the concentration of NADH at the electrode surface at time t. The $\Gamma_{ox,i}(t)$ is given by eq (3.13) with use of eqs (3.6) and (3.7).

$$\Gamma_{ox,i}(t) = \frac{\Gamma_i}{1+\exp\left[-(nFg_i / RT)(E(t) - E_i^{o'})\right]} \tag{3.13}$$

$j_{cat}(t)$ is also correlated to the flux of NADH at electrode surface ($r = r_0$) by eq (3.14).

$$\frac{j_{cat}(t)}{2F} = D_{NADH}\left(\frac{\partial c_{NADH}(r,t)}{\partial r}\right)_{r=r_0} \tag{3.14}$$

where D_{NADH} is the diffusion coefficient of NADH, r is the distance from the center of a wire electrode, and r_0 is the radius of the wire electrode used in the present study. Under our experimental conditions, the mass transport of NADH obeys a cylindrical diffusion, which is given by eq (3.15)

$$\frac{\partial c_{NADH}(r,t)}{\partial t} = D_{NADH}\left\{\frac{\partial^2 c_{NADH}(r,t)}{\partial r^2} + \frac{1}{r}\frac{\partial c_{NADH}(r,t)}{\partial r}\right\} \tag{3.15}$$

The explicit finite difference calculations [40] were then applied to eq (3.15) to evaluate $j_{cat}(t)$ with combining eqs (3.12) through (3.14). For these calculations, 2.191 x 10^{-4} cm and 0.01 s were chosen as the width of each volume element in the discretized diffusion layer and the time increment for each iteration, respectively. It was confirmed that these values were small enough to obtain convergence. $c_{NADH}(\infty, t)$ = 1 mmol dm^{-3} (concentration of NADH in bulk solution) and D_{NADH} = 2.4 x 10^{-6} cm^2s^{-1} [42] were used for the calculations.

Figure 3.9 shows the experimentally obtained voltammograms of the Th/Au, AzC/Au and AzA/Au electrodes taken in the electorolyte solution containing 1 mmol dm^{-3} NADH and the best fitted simulation curves which were obtained with use of the parameters summarized in Table 3.1. In this table, $E^{o'}$ of each species dissolved in solution and k_h values obtained for chemical oxidation of NADH in the homogeneous system are also given for comparison. The simulation curves

Table 3.1

Formal potentials and the second-order reaction rate constant for oxidation of NADH

	Thionine	Azure C	Azure A
(Dissolved state)			
$E^{o'}$ (mV vs. Ag/AgCl) [a]	-120	-135	-165
k_h ($mol^{-1}dm^3s^{-1}$)[b]	64.2	39.8	11.8
(Immobilized state)			
$E_1^{o'}$ (mV vs. Ag/AgCl)	-30	-45	-85
Γ_1 (10^{-10}mol cm^{-2})	0.58	0.40	0.40
$E_2^{o'}$ (mV vs. Ag/AgCl)	240	230	210
Γ_2 (10^{-10}mol cm^{-2})	1.2	0.70	0.49
$k_{c,2}$ ($10^5 mol^{-1}dm^3s^{-1}$)	1.2	0.95	0.55

a; The formal potential estimated from the midpoint between the cathodic and anodic peak potentials of cyclic voltammogram in 0.1 mol dm^{-3} phosphate buffer (pH 7.0) at a glassy carbon electrode.

b; Estimated from the absorbance change at 600 nm of 0.1 mol dm^{-3} phosphate buffer (pH 7.0) containing 50 mmol dm^{-3} NADH and 50 mmol dm^{-3} phenothiazine derivatives.

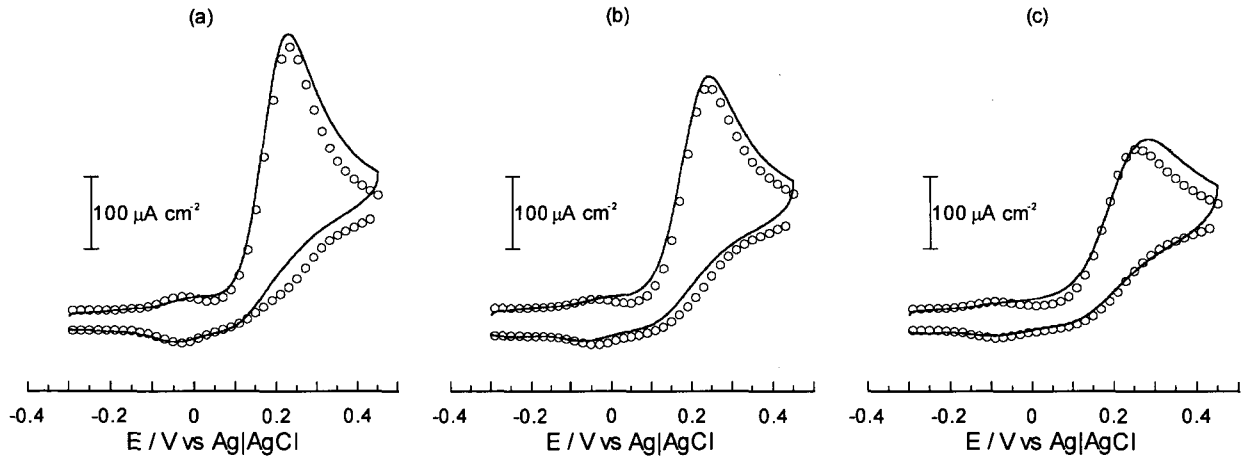

Figure 3.9

Experimentally obtained cyclic voltammograms (—) of the Th/Au (a), the AzC/Au (b), and the AzA/Au (c) electrodes taken in 1 mmol dm^{-3} NADH at 200 mV s^{-1} and best fitting simulated ones (○) to each voltammogram. g_i values (i = 1, 2) used in the simulation were 0.4 for all cases. Other parameters used in the simulation are given in Table 3.1.

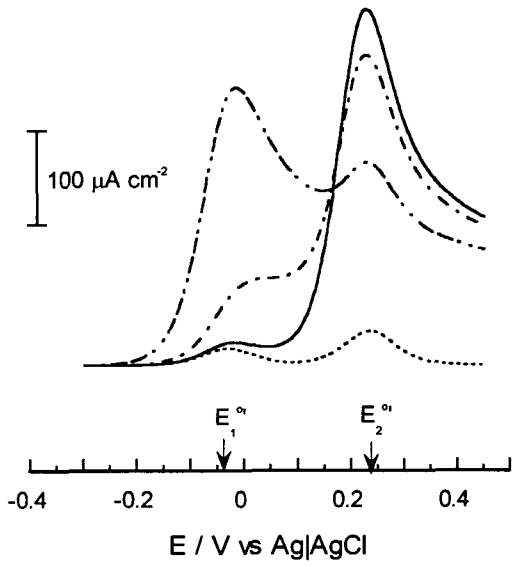

Figure 3.10

Simulated anodic waves of the Th/Au obtained by using $k_{c,1}$ of $1x10^3$(—), $1x10^4$(— - —), and $1x10^5$(— - - —) $mol^{-1}dm^3s^{-1}$. $k_{c,2}$ is fixed to be 1.2 x 10^5 mol^{-1} dm^3 s^{-1} and other parameters are the same as those used in Figure 3.10. Blank curve (- - -) was obtained by calculation of eq (3.10).

shown in Figure 3.9 were obtained by assuming that $k_{c,1}$ was the same for three kinds of electrodes used and it was 1 x 10^2 mol^{-1} dm^3 s^{-1}. This assumption is rationalized in the following way. As shown in Figure 3.10 for the case of the Th/Au electrode, if $k_{c,1}$ values larger than 1 x 10^3 mol^{-1} dm^3 s^{-1} was used in the simulation, the obtained voltammograms gave an anodic peak at around $E_1^{o'}$, and the peak became large with increasing $k_{c,1}$. It was found that use of $k_{c,1}$ = 1 x 10^2 $mol^{-1}dm^3$ s^{-1} gave a very good fitted shape of the voltammogram to the experimentally obtained one around $E_1^{o'}$ for all the simulation. Values of $k_{c,2}$ were then chosen so as to give the best fitted voltammogram with use of this $k_{c,1}$ value. As shown in Table 3.1, the second-order reaction rate constant of the catalytic oxidation of NADH ($k_{c,2}$) obtained for the Th/Au was (1.2 ± 0.1) x 10^5 mol^{-1} dm^3 s^{-1}. This value is larger than the highest rate constant reported so far for oxidation of NADH which was obtained with use of 3,4,-dihydroxybenzylamine [4] as a catalytic reagent ((7.7 ± 0.8) x 10^4 mol^{-1} dm^3 s^{-1}). The uncertainty of the obtained $k_{c,2}$ results in shifts of simulated peak potential of as small as ± 5mV.

An attempt was also made to simulate the voltammogram obtained by the electrocatalytic oxidation of NADH using the Th(r)/Au electrode, as shown in Figure 3.8. The catalytic currents exhibited two shoulders at around 0.1 and 0.3 V vs. Ag|AgCl in the positive potential scan, suggesting that there were two kinds of species which worked as electrocatalysts. However, only one pair of redox waves was observed in the voltammogram of the Th(r)/Au taken in the absence of NADH, as already shown in Figure 3.4, making it rather difficult to clarify the nature of the two kinds of shoulders observed. If assumptions were made that one kind of redox couple observed in the cyclic voltammogram shown in Figure 3.4 worked as an electrocatalyst and caused an increase in the oxidation currents at potentials positive of 0.1 V vs. Ag|AgCl, the simulation curves given by open

circles in Figure 3.8 were obtained with the use of parameters of Γ_1=1.3 x 10^{-10} mol cm^{-2}, $E_1^{o'}$= -0.03V vs. Ag|AgCl, $k_{c,1}$ = 1 x 10^2 mol^{-1} dm^3 s^{-1} and g_1 = 0.3. Apparently, the simulation curves deviate greatly from the experimentally obtained voltammograms. It is speculated that even with the use of the Th(r)/Au electrode a very small amount of the dimer, which could not be detected by cyclic voltammetry, was immobilized on the electrode surface, and the appearance of the two current shoulders are due to the contribution of both monomer and dimer.

Figure 3.11 shows the second-order rate constant of the catalytic oxidation of NADH obtained at immobilized dimeric species of thionine, azure C, and azure A as a function of the Gibbs energy changes (ΔG^o) for the oxidation reaction of NADH, which were evaluated by the redox potential of immobilized electrocatalysts and NADH. Also included in this figure are the rate constants obtained by other investigators with use of monolayer-coated electrodes of 1-amino-3,4,-benzoquinone [4], 3-hydroxytyramine [4], 4-methyl-1,2-benzoquinone [4], 1,2,-naphtoquinone-4-sulfonic acid [6], poly(thionine) [13], and PQQ [27], which are given by open circles. As this figure shows, a linear free-energy relation is maintained even if the redox species are immobilized on electrodes. Since ΔG^o of NADH oxidation with the monomeric form of thionine, azure C, and azure A immobilized on the electrode are estimated to be -98.5, -95.5, and -87.8 kJ mol^{-1}, respectively, determined with use of their formal potentials, the second-order reaction rate constants with use of these monomers ($k_{c,1}$) must be ca. 10^2 mol^{-1} dm^3 s^{-1}, as judged from the results shown in Figure 3.11. It is noticed by

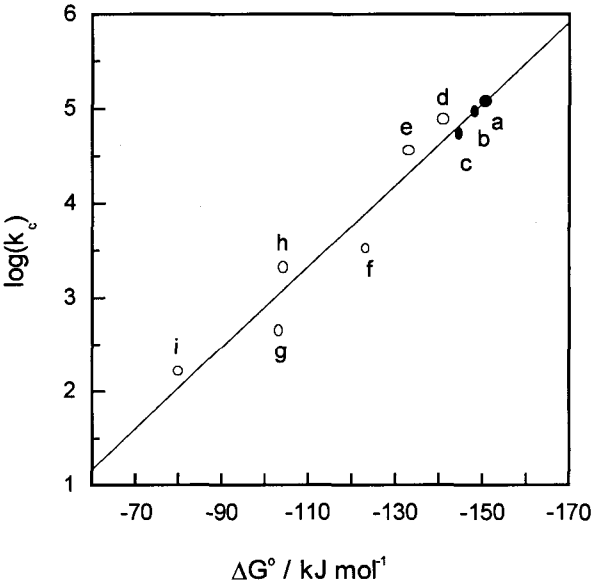

Figure 3.11

Relationship between logarithm of the second-order reaction rate constants and the Gibbs energy change obtained for electron exchange between NADH and dimeric Th/Au (a)α, dimeric AzC/Au (b)α, dimeric AzA/Au (c)α, 1-amino-3,4,-benzoquinone/carbon (d)β, 3-hydroxytyramine/carbon (e)β, 4-methyl-1,2-benzoquinone/carbon (f)β, 1,2,-naphthoquinone-4-sulfonic acid/carbon (g)χ, poly(thionine)/carbon (h)δ, and PQQ/Au (i)ε electrode. α:Measured in this work. β:From ref. 4. χ:From ref. 6. δ:From ref. 13. ε:From ref. 25.

comparing the reaction rate constants between dissolved phenotiazine derivatives and immobilized ones, which are given in Table 3.1, that the reaction rate is enhanced by a factor of more than 10^4 by immobilization of the phenothiazine derivatives on the electrode. As has been reported [11, 12] and mentioned above, the redox potential of the 3-amino-derivatives of phenothiazine is shifted positively by conversion of an amino group to an amide group. Furthermore, a positive shift of the redox potential occurs with dimerization of the phenothiazine derivatives. Such positive shifts of the redox potentials enhance the thermodynamic driving force of the electrochemical oxidation of NADH. As shown in Figure 3.11, the apparent activities for electrochemical of NADH are controlled by the Gibbs energy difference between the electrocatalyst and NADH. The results may suggest that the use of the term of electrocatalyst is not sound for the substances given in this figure for NADH oxidation, because the electrocatalysts should show high activities for reactions of interest with an activation energy as small as possible. However, it is also true that redox reagents having thermodynamically large driving forces for NADH oxidation do not always show activities for the oxidation of NADH. In this sense, the phenothiazine derivatives used in this study are said to work as electrocatalysts.

3.4 REFERENCES

1. A. P. F. Turner, I. Karube, and G. S. Wilson(ed.), Biosensors-Fundamentals and Applications, Oxford University Press, Oxford, 1987.
2. W. J. Blaedel and R. A. Jekins, *Anal. Chem.*, **47** (1975) 1337.
3. Z. Samec and P.J. Elving, *J. Electroanal. Chem.*, **144** (1983) 217.
4. D.C-S. Tse and T. Kuwana, *Anal.Chem.*, **50** (1978) 1315.
5. H. Jaegfeldt, A.B.C. Trstensson, L.G.O. Gorton and G. Johansson, *Anal. Chem.*, **53** (1981)1979.
6. R.F. Lane and A.T. Hubbard, *Anal. Chem.*, **48** (1976) 1287.
7. M. Fukui, A. Kitani, C. Degrand and L.L. Miller, *J. Am. Chem. Soc.*, **104** (1982) 28.

8. H. Jaegfeldt, T. Kuwana and G. Johansson, *J. Am. Chem. Soc.*, **105** (1983) 1805.
9. F. Pariente, E. Lorenzo and H.D. Abruna, *Anal. Chem.*, **66** (1994) 4337.
10. L. Gorton, A. Torstensson, H. Jaegfeldt and G. Johansson, *J. Electroanal. Chem*, **161** (1984) 103.
11. B. Persson, *J. Electroanal. Chem*, **287** (1990) 61.
12. B. Persson and L. Gorton, *J. Electroanal. Chem*, **292** (1990) 115.
13. T. Ohsaka, K. Tanaka and K. Tokuda, *J. Chem. Soc., Chem. Commun.*, (1993) 222.
14. T. Ohsaka, K. Tanaka and K. Tokuda, *J. Chem. Soc., Chem. Commun.*, (1993) 1770.
15. A.A. Karyakin, E.E. Karyakina, W. Shuhmann, H.L. Schmidt, and S.D. Varfolomeyev, *Electroanalysis*, **6** (1994) 821.
16. A. Ulman, An Introduction to Ultrathin Organic Films, Academic Press, San Diego, CA, 1991, Part Three.
17. C.E.D. Chidsey, C.R. Bertozzi, T.M. Putvinski, and A.M. Mujsce, *J. Am. Chem. Soc.* **112** (1990) 4301.
18. H.C.D. Long and D.A. Buttry, *Langmuir*, **6** (1990) 1319.
19. M. Collinson and E. F. Bowden, *Langmuir*, **8**(1992)1247.
20. I. Willner, A. Riklin, B. Shoham, D. Rivenzon, and E. Katz, *Adv. Mater.*, **5**(1993)912.
21. E. Katz, A. Riklin, and I. Willner, *J. Electroanal. Chem.*, **354** (1993) 129.
22. E. Katz, N. Itzhak, and I. Willner, *Langmuir*, **9**(1993)1392.
23. M. Lion-Dagan, E. Katz, and I. Willner, *J. Am. Chem. Soc.*, **116**(1994)7913.
24. E. Katz, D.D. Schlereth, and H.L. Schmidt, *J. Electroanal. Chem.*, **367** (1994) 59.
25. E. Katz, D.D. Schlereth, H.L. Schmidt, and A.J.J. Olsthoorn, *J. Electroanal. Chem.*, **368** (1994) 165
26. D.D. Schlereth and H.L. Schmidt, *J. Electroanal. Chem.*,**380** (1995) 117.
27. E. Katz, T. Lötzbeyer, D.D. Schlereth, W. Shuhmann and H.L. Schmidt, *J. Electroanal. Chem.*, **373** (1994) 189.
28. I. Willner and R. Riklin, *Anal. Chem.*, **66** (1994) 1535.
29. D.D. Schlereth, E. Katz and H.L. Schmidt, *Electroanalysis*, **6** (1994) 725.
30. D.D. Schlereth, E. Katz, and H.L. Schmidt, *Electroanalysis*, **7** (1995) 46

31. E.Y. Katz, *J. Electroanal. Chem.*, **291** (1990) 257.

32. K. Burton and T.H. Wilson, *Biochem. J.*, **54** (1953) 86.

33. D.B. Rifkin, R.W. Compans, and F. Reich, *J. Biol. Chem.*, **247** (1972) 6432.

34. E. Rabinowith and L.F. Epstein, *J. Am. Chem. Soc.*, **63** (1941) 69.

35. H. Huck, Z. *Anal. Chem.*, **313** (1982) 548.

36. S.E. Creager and G.K. Rowe, *J.Phys. Chem.*, **98** (1994) 5500.

37. E. Laviron, *J. Electroanal. Chem.*, **101** (1979) 19.

38. Y. Xie and F.C. Anson, *J. Electroanal. Chem.*, **384** (1995) 145.

39. C.P. Andrieux and J.M. Saveant, *J. Electroanal. Chem.*, **93**(1978)163.

40. S.W. Feldberg, in A.J. Bard (ed.), *Electroanalytical Chemistry*, Vol. 3, Marcel Dekker, New York, 1969.

41. K. Aoki, K. Tokuda, and H. Matsuda, *J. Electroanal. Chem.*, **199**(1986)69.

42. M. Aizawa, R.N. Coughlin, and M. Charles, *Biochem. Biophys. Acta*, **385**(1975) 362.

chapter 4

Voltammetric Response Accompanied by Inclusion of Ion-pairs and Triple Ions Formation of Electrodes Coated with an Electroactive Monolayer Film

4.1 INTRODUCTION

Electrochemistry of self-assembled monolayers (SAM) having redox active groups has been getting great interests in recent years [1-12]. Theory on cyclic voltammetry on such surface-confined redox species has been developed with use of the Langmuir adsorption isotherm and the Nernst equation [13]. However, the shape of experimentally obtained voltammograms are often much broader [1,2,7,9] than that predicted by the theoretical predictions, and in some cases spiky redox waves appear [5,11]. Furthermore, it has been found that the apparent formal potential is apt to shift especially when the surface concentration of surface-confined redox species is high [1,2,7]. Such non-ideal voltammetric behaviors were first theoretically treated by Laviron who introduced adjustable interaction parameters to make good matching of experimentally obtained voltammograms to the theoretically obtained ones [14-16]. Recently White and Smith analyzed voltammetric behaviors of an electrode coated with redox active SAM and showed that the broadening of voltammetric waves and shifts of their apparent formal potentials can also be explained without any empirical adjustable parameter if potential drops across the SAM are taken into consideration [17]. Their theoretical treatments were further refined with inclusion of "discreteness-of-charge effects" [18,19], and applied to other electrochemical problems in which the potential-dependent acid/base equilibrium of a SAM [20,21] and the potential-induced orientation of an amphiphilic molecule [22] were taken into consideration.

In this chapter, further refinements of the theoretical treatments made by Smith and White

[17] are made in terms of formation of ion-pairs and triple ions between redox active SAM and electrolyte ions. The ion-pair formation is suggested from the finding that the voltammetric peak obtained at electrodes coated with SAM of alkylthiol derivatives of ferrocene was varied with changes in the concentration of electrolyte solution [3,7,11]. Furthermore, *in-situ* measurements using the EQCM (electrochemical quartz crystal microbalance) technique of electrodes coated with SAM of alkylthiol derivatives of ferrocene [11] and viologen [12] revealed the occurrence of association and dissociation of electrolyte ions with surface-confined redox species during the course of the redox processes. A potential distribution profile considered in the original work by Smith and White [17] is shown in Figure 4.1 (A), where no ion-pair formation was assumed for surface-confined species. If the same surface-confined species interacts strongly with the electrolyte counter anions, a potential distribution profile as shown in Figure 4.1 (B) seems valid. The potential difference between the electrode substrate and the solution bulk is concentrated in the SAM. If the surface-confined positively charged species is subjected to excessive compensation such as with triple ions formation, the potential drop in the SAM is increased, as shown in Figure 4.1 (C), which is also valid for metal electrodes having specific adsorption of electrolyte anions [23]. If such changes in the potential distributions occur in the redox reactions of the surface-confined electroactive species, not only the peak potential but also the shape of voltammograms

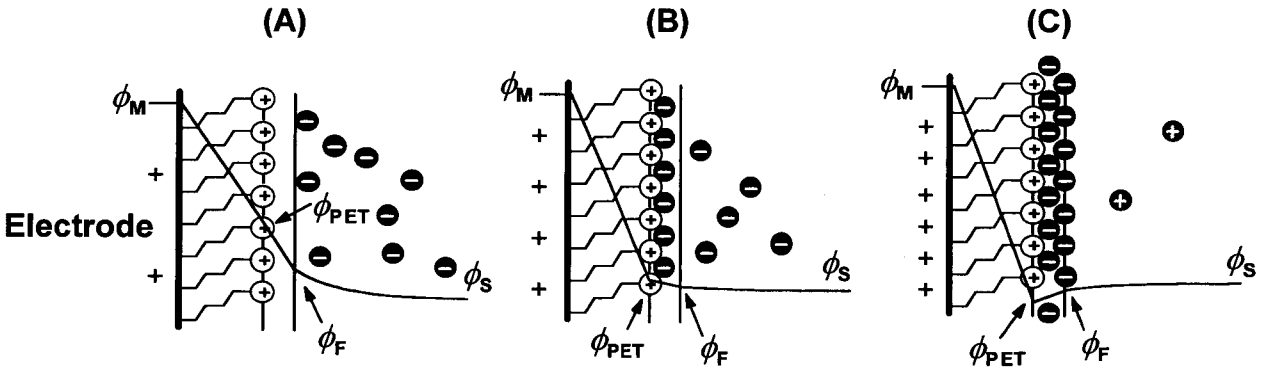

Figure 4.1

Schematic illustration of potential distributions across solution/SAM/electrode substrate interface. The zig-zag line indicates a dielectric film like alkyl chain and the signs (+,-) denote the charges of electrode substrate surface, surface-confined species, and the electrolyte ions. (A): For a case for insufficient compensation of surface-confined positive charges with electrolyte anions, (B): as in (A), but for full neutralization, (C): as in (A), but for excessive accumulation of electrolyte anions. The parameters given in the figure are described in the text.

will be changed depending on the degree of interaction of electroactive SAM with electrolyte ions. In this chapter, explicit solutions for the peak current and the peak potential of the voltammetric waves are presented, discussion is made to correlate them with the Laviron's treatments [14,15], and a graphical method to evaluate the double-layer effects is proposed.

4.2 THEORY

4.2.1 Model and Potential Distribution across Monolayer and Double Layer

Figure 4.2 shows an interfacial structure model of a plane electrode coated with a redox active SAM having thickness d_1 and dielectric constant ε_1. The redox group is located at the end of

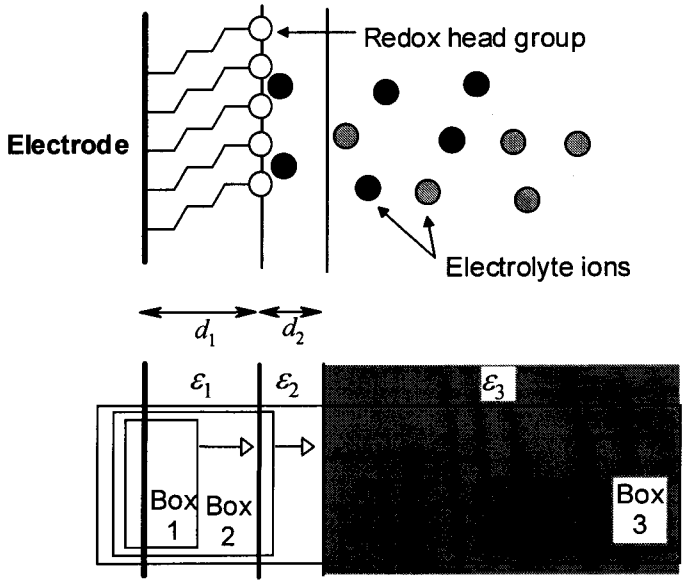

Figure 4.2

Schematic illustration of a solution/SAM/electrode substrate interface (upper) and the model system used to calculate the potential profile (lower). The zig-zag line given in the upper figure indicates a dielectric film like alkyl chain, open circles are redox group, closed and gray circles are electrolyte ions. σ_M and σ_{PET} are delocalized on the electrode surface at x=0 and the inner Helmholtz plane at x=d_1, respectively. Boxes 1, 2, and 3 denote for regions covering from the electrode substrate to the inner Helmholtz layer, for those to the outer Helmholtz layer, and for those to electrolyte solution bulk, respectively, and the Gauss' law was applied to them to correlate the electric field to the charge density.

SAM ($x=d_1$). The distance between the inner and the outer Helmholtz plane is d_2 in which a medium of the dielectric constant ε_2 is filled. The dielectric constant of the solution phase is given by ε_3. The charges on the metal electrode surface at $x=0$ are given by σ_M, and those on the inner Helmholtz plane at which the redox head groups are presented are given by σ_{PET}. The inner Helmholtz plane is denoted here as PET. It is assumed that both σ_M and σ_{PET} are delocalized in each plane, i.e., the discreteness-of-ion effect [18] is ignored as assumed by Smith and White [17]. This means that even if the ion-pairs and triple ions are formed, their charges are also delocalized on the PET. It is further assumed that there are no net charges in the region of $0<x<d_1$ and $d_1<x<d_1+d_2$, and the volume charge density in the diffuse layer ($x>d_1+d_2$) is given by $\rho(x)$.

In order to correlate the electric fields to the charge densities of interest with using the Gauss' law, boxes 1, 2, and 3 are imagined for the inner Helmholtz region, the region covering up to the outer Helmholtz region, and that extending to the solution bulk, respectively, as shown in Figure 4.2. Application of the Gauss' law to the boxes 1 and 2 gives

$$\varepsilon_1\varepsilon_0 E_1 = \sigma_M \qquad \text{(Box 1)} \qquad (4.1a)$$

$$\varepsilon_2\varepsilon_0 E_2 = \sigma_M + \sigma_{PET} \qquad \text{(Box 2)} \qquad (4.1b)$$

where E_1 and E_2 are the magnitude of the electric field in the region of $0<x<d_1$ and $d_1<x<d_1+d_2$, respectively, and ε_0 is the permittivity of vacuum (8.854×10^{-12} $J^{-1}C^2m^{-1}$). Indefinite integration of eq (4.1a) with respect to the distance from the electrode surface (x) using the relation of $E_j=-d\phi(x)/dx$ gives

$$\int \frac{d\phi(x)}{dx}dx = -\int \frac{\sigma_M}{\varepsilon_1\varepsilon_0}dx \qquad (4.2)$$

Then, the average local potential, $\phi(x)$, as a function of x can be given by

$$\phi(x) = -\frac{\sigma_M x}{\varepsilon_1\varepsilon_0} + B_1 \qquad d_1 > x > 0 \qquad (4.3a)$$

Similarly, eq (4.3b) is derived from eq (4.1b)

$$\phi(x) = -\frac{(\sigma_M + \sigma_{PET})x}{\varepsilon_2 \varepsilon_0} + B_2 \qquad d_1 + d_2 > x > d_1 \qquad (4.3b)$$

where B_1 and B_2 are integration constants whose values are determined so as to maintain the continuity of the potential distribution at d_1 and d_1+d_2, respectively. Since most of the potential drops should occur within the organic layer due to its low dielectric constant, the potential at the outer Helmholtz layer, ϕ_F, at the distance of $x = d_1$+d_2 relative to the potential of the bulk electrolyte solution must be equal to or smaller than ca. 50 mV, as already discussed by White and Smith [17]. Then, the potential distribution in the diffuse layer (x>d_1+d_2) can be estimated using the following relation [13, 24]

$$\phi(x) = \phi(d_1 + d_2)e^{-\kappa(x-d_1-d_2)} \qquad x > d_1 + d_2 \qquad (4.4)$$

where κ is the Debye-Hückel reciprocal length which is given by $\kappa = zF(2C/\varepsilon_3\varepsilon_0 RT)^{1/2}$ for a symmetric z: z electrolyte solution with the concentration of C. The volume charge density in the diffuse layer, $\rho(x)$, is related to $\phi(x)$ by the Poisson's equation.

$$\frac{d^2\phi(x)}{dx^2} = -\frac{\rho(x)}{\varepsilon_3 \varepsilon_0} \qquad (4.5)$$

The application of the Gauss' law to the box 3 given in Figure 4.2 yields the following relation by taking into consideration of the charge neutrality,

$$\sigma_M + \sigma_{PET} + \sigma_{dif} = \sigma_M + \sigma_{PET} + \int_{d_1+d_2}^{\infty} \rho(x)dx = 0 \qquad (4.6)$$

where σ_{dif} refers to the net electric charge of the entire diffuse layer. Combining eqs (4.4), (4.5) and (4.6) with each other, the potential in the diffusion layer is described by

$$\phi(x) = \frac{(\sigma_M + \sigma_{PET})\exp[\kappa(d_1 + d_2 - x)]}{\varepsilon_3 \varepsilon_0 \kappa} \qquad d_1 + d_2 \le x \qquad (4.7a)$$

It should be noted that $\phi(x)$ gives the potential relative to the potential of the bulk electrolyte solution (ϕ_S=0). By determining B_2 in eq (4.1b) in such a way as to satisfy the continuity of the potential at x=d_1+d_2, then B_1 in eq (4.1a) is determined with consideration of the continuity of the potential at x=d_1. In this way, the potential in a region between the outer Helmholtz layer and the electrode substrate is obtained which are given by eqs (4.7b) and (4.7c), respectively.

$$\phi(x) = \left(\frac{d_1 + d_2 - x}{\varepsilon_2 \varepsilon_0} + \frac{1}{\varepsilon_3 \varepsilon_0 \kappa}\right)(\sigma_M + \sigma_{PET}) \qquad d_1 \le x \le d_1 + d_2 \quad (4.7b)$$

$$\phi(x) = \frac{(d_1 - x)\sigma_M}{\varepsilon_1 \varepsilon_0} + \left(\frac{d_2}{\varepsilon_2 \varepsilon_0} + \frac{1}{\varepsilon_3 \varepsilon_0 \kappa}\right)(\sigma_M + \sigma_{PET}) \qquad 0 \le x \le d_1 \quad (4.7c)$$

4.2.2 Voltammetric Response of One-electron Reversible System Involving Formation of Ion-pairs and Triple Ions

Let a one-electron reversible redox reaction of surface-confined redox couple, O^+/R^0 like ferricinium/ferrocene couple be given by

$$O^+ + e^- \rightleftarrows R^0 \qquad (4.8)$$

The redox couple in an equilibrium state gives the following relationship [17].

$$\phi_M - \phi_{PET} = E^o - E_{pzc} - \frac{RT}{F}\ln\left(\frac{\Gamma_{R^0}}{\Gamma_{O^+}}\right) \qquad (4.9)$$

where ϕ_M is the inner potential of the metallic electrode, ϕ_{PET} is the potential at the PET ($x=d_1$), E^o is the standard potential of a redox couple, E_{pzc} is the potential of zero charge of the substrate electrode, Γ_{O^+} and Γ_{R^0} are the surface concentration of O^+ and R^0, respectively, and R, T, and F have their usual significance.

As described already above, the EQCM studies on the redox active SAM of ferrocene [11] and viologen [12] derivatives showed that when electrochemical oxidation of the monolayer occurs, electrolyte anions are bound to the electrode. In the electrolyte solutions, the formation of ion-pairs and triple ions may be formulated by eqs (4.10a), (4.10b), and (4.10c)

(Ion pair) $$C^+ + A^- \rightleftarrows (CA)^0 \qquad (4.10a)$$

(Triple ions) $$(CA)^0 + A^- \rightleftarrows (CA_2)^- \qquad (4.10b)$$

$$(CA)^0 + C^+ \rightleftarrows (C_2A)^+ \qquad (4.10c)$$

where C^+ and A^- denote cationic and anionic species, respectively [25-29], and the formation of triple ions becomes marked with increasing the concentration of electrolytes especially when the solvent has a low dielectric constant [25-29]. When cationic species are generated on the SAM with a high density in the redox reaction, the ion-pair and triple ion formation as given by eqs (4.11a) and (4.11b) seems easy to occur at PET, because the electrode substrate/solution interface in such cases gives a lower dielectric environment than that of the bulk solution [30].

$$O^+ + X^- \rightleftarrows (OX)^0 \tag{4.11a}$$

$$(OX)^0 + X^- \rightleftarrows (OX_2)^- \tag{4.11b}$$

The equilibrium constants of the formation of $(OX)^0$ and $(OX_2)^-$, which are denoted here as K_{o1} and K_{o2}, respectively, are defined by

$$K_{o1} = \frac{\Gamma_{(OX)^0}}{\Gamma_{O^+}[X^-]_S} \tag{4.12a}$$

$$K_{o2} = \frac{\Gamma_{(OX_2)^-}}{\Gamma_{(OX)^0}[X^-]_S} \tag{4.12b}$$

where Γ_i is the surface concentration of species i at PET and $[X^-]_S$ is the concentration of X^- in the bulk solution that is equal to the concentration of the supporting electrolyte (C). Note that K_{o1} and K_{o2} are tacitly assumed to be independent on the potential. The surface concentration of the redox active group in the oxidized state is, then, given by

$$\Gamma_{O^+} + \Gamma_{(OX)^0} + \Gamma_{(OX_2)^-} = \Gamma_{O^+}\left(1 + CK_{o1} + C^2 K_{o1} K_{o2}\right) \tag{4.13}$$

Combining eqs (4.9), (4.12a), and (4.12b) yields

$$\phi_M - \phi_{PET} = E^\circ - E_{pzc} - \frac{RT}{F}\ln\left\{\frac{\Gamma_{R^0}\left(1 + CK_{o1} + C^2 K_{o1} K_{o2}\right)}{\Gamma_{O^+} + \Gamma_{(OX)^0} + \Gamma_{(OX_2)^-}}\right\} \tag{4.14}$$

The fraction of the redox active species in the oxidized states is given by

$$f = \frac{\Gamma_{O^+} + \Gamma_{(OX)^0} + \Gamma_{(OX_2)^-}}{\Gamma_T} \tag{4.15}$$

where Γ_T is the total surface concentration of the redox species ($\Gamma_T = \Gamma_{O^+} + \Gamma_{(OX)^0} + \Gamma_{(OX_2)^-} + \Gamma_{R^0}$). By substituting eqs (4.13) and (4.15) into eq (4.14), eq (4.16) which includes K_{o1} and K_{o2} is obtained.

$$\phi_M - \phi_{PET} = E^\circ - E_{pzc} - \frac{RT}{F}\ln\left(1 + CK_{o1} + C^2 K_{o1}K_{o2}\right) - \frac{RT}{F}\ln\left\{\frac{1-f}{f}\right\} \tag{4.16}$$

Eq (4.16) is solved for f with the use of eqs (4.7b) and (4.7c) (i.e., $\phi_M = \phi(0)$, $\phi_{PET} = \phi(d_1)$) to give

$$f = \frac{1}{1 + K'\exp\left[\frac{F}{RT}\left\{E^\circ - E_{pzc} - (\phi_M - \phi_{PET})\right\}\right]} = \frac{1}{1 + K'\exp\left[\frac{F}{RT}\left(E^\circ - E_{pzc} - \frac{\sigma_M d_1}{\varepsilon_1 \varepsilon_0}\right)\right]} \tag{4.17}$$

where

$$K' = \frac{1}{1 + CK_{o1} + C^2 K_{o1}K_{o2}} \tag{4.18}$$

The charge density at PET (σ_{PET}) is given by

$$\sigma_{PET} = F\Gamma_T\left\{z_O f + z_R(1-f)\right\} \tag{4.19}$$

where z_O is referred to the net ionic charge of the oxidized states, which is given by

$$z_O = \frac{\Gamma_{O^+} - \Gamma_{(OX_2)^-}}{\Gamma_{O^+} + \Gamma_{(OX)^0} + \Gamma_{(OX_2)^-}} = \frac{1 - C^2 K_{o1}K_{o2}}{1 + CK_{o1} + C^2 K_{o1}K_{o2}} \tag{4.20}$$

and z_R is the net ionic charge of the reduced state. Although z_R is 0 in the present case, it is consciously included in the equations for the purpose of general discussion. If the redox active species in the reduced state also has any charges, the formation of its ion pairs and triple ions must be taken into account, using the same procedure as those used for z_O mentioned above. By combining eqs (4.17) with (4.19), a relation between σ_{PET} and σ_M, as given by eq (4.21), is obtained.

$$\sigma_{PET} = F\Gamma_T\left\{z_R + \frac{z_O - z_R}{1 + K'\exp\left[\frac{F}{RT}\left(E^\circ - E_{pzc} - \frac{\sigma_M d_1}{\varepsilon_1 \varepsilon_0}\right)\right]}\right\} \tag{4.21}$$

Since the applied electrode potential (E) is the sole parameter which can be externally controlled, it is useful to combine the above descriptions with E using the following relation

$$\phi(0) = \phi_M - \phi_S = (\phi_M - \phi_{ref}) - (\phi_S - \phi_{ref}) = E - E_{pzc} \tag{4.22}$$

where ϕ_{ref} is the potential of the reference electrode. Substitution of eqs (4.21) and (4.22) into eq (4.7a) yields

$$\left(\frac{d_1}{\varepsilon_1\varepsilon_0} + \frac{d_2}{\varepsilon_2\varepsilon_0} + \frac{1}{\varepsilon_3\varepsilon_0\kappa}\right)\sigma_M + F\Gamma_T\left(\frac{d_2}{\varepsilon_2\varepsilon_0} + \frac{1}{\varepsilon_3\varepsilon_0\kappa}\right)\left\{z_R + \frac{z_O - z_R}{1 + K'\exp\left[\frac{F}{RT}\left(E^o - E_{pzc} - \frac{\sigma_M d_1}{\varepsilon_1\varepsilon_0}\right)\right]}\right\} - E + E_{pzc} = 0 \tag{4.23}$$

Then, the faradaic current is described in the following way.

$$i_f = FA\Gamma_T\frac{df}{dt} = FA\Gamma_T\left(\frac{df}{d\sigma_M}\right)\left(\frac{d\sigma_M}{dE}\right)\frac{dE}{dt} = FAv\Gamma_T\left(\frac{df}{d\sigma_M}\right)\left(\frac{d\sigma_M}{dE}\right) \tag{4.24}$$

where A is the electrode area, and v is the potential sweep rate. $(df/d\sigma_M)$ and $(d\sigma_M/dE)$ are obtained by differentiations of eqs (4.17) and (4.23), respectively

$$\frac{df}{d\sigma_M} = \frac{F\left(\frac{d_1}{\varepsilon_1\varepsilon_0}\right)K'e^{\eta}}{RT\left(1 + K'e^{\eta}\right)} \tag{4.25}$$

$$\frac{d\sigma_M}{dE} = \frac{1}{\left(\frac{d_1}{\varepsilon_1\varepsilon_0} + \frac{d_2}{\varepsilon_2\varepsilon_0} + \frac{1}{\varepsilon_3\varepsilon_0\kappa}\right) + \frac{(z_O - z_R)F^2\Gamma_T\left(\frac{d_2}{\varepsilon_2\varepsilon_0} + \frac{1}{\varepsilon_3\varepsilon_0\kappa}\right)\left(\frac{d_1}{\varepsilon_1\varepsilon_0}\right)K'e^{\eta}}{RT\left(1 + K'e^{\eta}\right)^2}} \tag{4.26}$$

where

$$\eta = \frac{F}{RT}\left(E^o - E_{pzc} - \frac{\sigma_M d_1}{\varepsilon_1\varepsilon_0}\right) \tag{4.27}$$

The faradaic current is obtained as a function of σ_M by substituting eqs (4.25) and (4.26) into eq (4.24).

$$i_f = \frac{F^2 A v \Gamma_T K' e^{\eta}}{RT\left(1+K'e^{\eta}\right)^2\left(1+\frac{\varepsilon_1 d_2}{\varepsilon_2 d_1}+\frac{\varepsilon_1}{\varepsilon_3 \kappa d_1}\right)+\left(z_O - z_R\right)F^2\Gamma_T\left(\frac{d_2}{\varepsilon_2\varepsilon_0}+\frac{1}{\varepsilon_3\varepsilon_0\kappa}\right)K'e^{\eta}} \tag{4.28}$$

Although it is necessary to calculate σ_M as a function of E using eq (4.23) to obtain whole current-voltage curves, the peak current and the peak potential are obtained straightforwardly if f is equal to 0.5. In that case, σ_M is given by eq (4.29) from eq (4.17).

$$\sigma_M = \frac{\varepsilon_1\varepsilon_0}{d_1}\left\{E^o - E_{pzc} + \frac{RT}{F}\ln(K')\right\} \tag{4.29}$$

Substituting eq (4.29) into eq (4.28), the peak current, $i_{f,peak}$, is given by

$$i_{f,peak} = \frac{F^2 A v \Gamma_T}{4RT\left(1+\frac{\varepsilon_1 d_2}{\varepsilon_2 d_1}+\frac{\varepsilon_1}{\varepsilon_3 \kappa d_1}\right)+\left(z_O - z_R\right)F^2\Gamma_T\left(\frac{d_2}{\varepsilon_2\varepsilon_0}+\frac{1}{\varepsilon_3\varepsilon_0\kappa}\right)} \tag{4.30}$$

The peak potential relative to the potential of zero-charge of the substrate electrode, E_{peak}-E_{pzc}, is obtained by substituting eq (4.29) into eq (4.23)

$$E_{peak} - E_{pzc} = \left\{E^o - E_{pzc} + \frac{RT}{F}\ln(K')\right\}\left(1+\frac{\varepsilon_1 d_2}{\varepsilon_2 d_1}+\frac{\varepsilon_1}{\varepsilon_3 \kappa d_1}\right)+\frac{\left(z_O + z_R\right)F\Gamma_T}{2}\left(\frac{d_2}{\varepsilon_2\varepsilon_0}+\frac{1}{\varepsilon_3\varepsilon_0\kappa}\right) \tag{4.31}$$

4.2.3 Numerical Calculation for Whole Current-Voltage Curves and Potential Distribution

The faradaic current of i_f given by eq (4.28) is a function of η which varies linearly with σ_M as given by eq (4.27). In order to investigate the variation of i_f as a function of E, σ_M must be obtained for a given E. Though there is a non-linear relationship between E and σ_M as given by eq (4.23), the computational calculations can be carried out using the Newton-Raphson method [29].

For this purpose, let the whole left hand side of eq (4.23) be represented by a function $g(\sigma_M)$. The problem is to find out a σ_M value for a specified E by iterating calculations until $\sigma_M^{(j+1)}$ becomes eventually equal to $\sigma_M^{(j)}$ using the following equation [29].

$$\sigma_M^{(j+1)} = \sigma_M^{(j)} - \frac{g(\sigma_M^{(j)})}{\left(\frac{\partial g(\sigma_M)}{\partial \sigma_M}\right)_{\sigma_M=\sigma_M^{(j)}}} \tag{4.32}$$

where superscript (j) is the iteration number. The calculation was carried out using $(\varepsilon_1\varepsilon_0 E)/d_1$ for an initial value of $\sigma_M^{(0)}$. Once σ_M is obtained for a given E, then, i_f, σ_{PET}, and f at E are obtained by using eqs (4.28), (4.21) and (4.17), respectively. A potential distribution profile for a given E is, in turn, obtained by substituting the obtained σ_{PET} and σ_M into eqs (4.7a-c).

Another method which is described below and was adopted in the work by Smith and White [17] is also applicable to draw a current-voltage curve. If a value of f is arbitrarily chosen, the corresponding σ_M value is obtained by with use of eq (4.17). Then, E and i_f can be evaluated by using eqs (4.23) and (4.28), respectively. It was confirmed that both methods gave completely the same voltammetric waves, as will be shown in the Results and Discussion.

4.3 RESULTS AND DISCUSSION

4.3.1 Current-Voltage Curves

To examine effects of the net charge at PET on the voltammetric behaviors, calculations were carried out using the following common parameters; E^o= 0.2 V vs. E_{pzc}, T = 298 K, d_1=0.9 nm, d_2=0.1 nm, ε_1=3, ε_2=12, ε_3=78.5. The dielectric constants of ε_1 and ε_3 chosen were those of typical values of aliphatic monolayers [30], and the bulk water [31], respectively, and ε_2 used was that reported for the secondary water layer [31]. The calculations were repeated until $g(\sigma_M^{(j)})/g'(\sigma_M^{(j)})$ became smaller than 10^{-9} C m^{-2} which was of convergence tolerance. If the potential in the diffuse

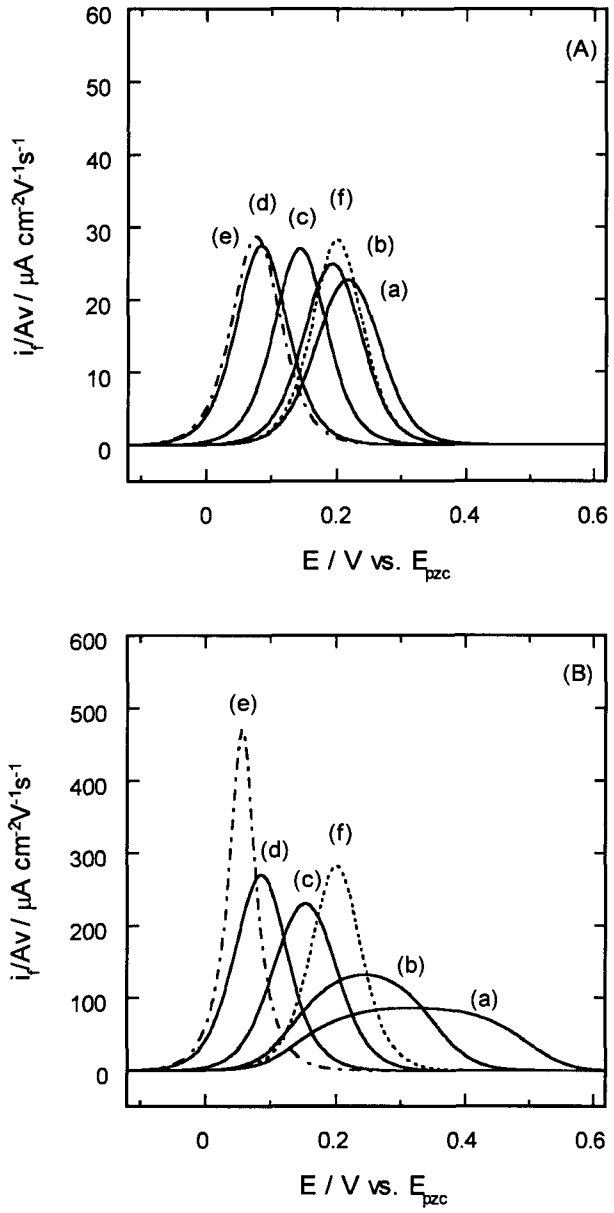

Figure 4.3

Calculated cyclic voltammograms of surface-confined redox species at (A) Γ_T =0.3x10^{-10} mol cm^{-2} and (B) Γ_T=3x10^{-10} mol cm^{-2}. (a)K_{o1}=K_{o2}=0, z_O=+1, (b) K_{o1}=1, K_{o2}=0, z_O =+0.5, (c) K_{o1}=10, K_{o2}=0, z_O =+0.09, (d) K_{o1}=100, K_{o2}=0, z_O =+0.01, (e, broken curve) K_{o1}=100, K_{o2} =0.25, z_O =-0.19, and (f, dotted curve) ideal Nernstian without ion-pairing. Other parameters are given in the text.

layer is given by an exponential function, the charging current is not large enough to distort the voltammogram. Therefore, the contribution of the charging current is not considered here. The expected voltammograms in that case are symmetric with respect to the peak potential. However, it seems important to note here that the shape of voltammograms is asymmetric with respect to the peak potential if the charging currents in the diffuse double layer cannot be ignored, as already discussed by White and Smith [17] based on eq (4A-1) given in Appendix of this chapter.

Figure 4.3 shows normalized voltammograms, which were obtained by dividing the current value by the product of electrode area and potential scan rate (*Av*). An ideal Nernstian type voltammogram of an one-electron reversible system without formation of any ion-pairs and triple ions is also given by dotted curve in Figure 4.3 for comparison, where the full width of half maxima (FWHM) is 90.6 mV (at 25 °C) [13]. Since the reversible system gives cathodic and anodic waves having a mirror image of each other, only anodic waves are shown in the figure. When the amount of surface-confined redox species is relatively low (Γ_T = 0.3 x 10^{-10} mol cm^{-2}), the shape of voltammogram is not greatly different from that of the ideal Nernstian

as shown in Figure 4.3 (A), but the peak potential is negatively shifted by decreasing the z_O values. On the other hand, when the amount of the surface-confined redox species is high (Γ_T = 3.0 x 10^{-10} mol cm^{-2}), the voltammetric wave is largely deviated from the ideal Nernstian in both the shape and the peak potential, as shown in Figure 4.3 (B). When the net ionic charge at PET (i.e., z_O) is positive, the peak currents decrease with increase in z_O and the width of the wave become broad, as shown by curves (a-c) in Figure 4.3 (B). If the positive charges of the redox active group are neutralized with electrolyte anions at PET, the shape of voltammetric wave becomes close to that of the ideal Nernstian as shown by curve (d) in Figure 4.3 (B), though the peak potential is different. The formation of triple ion $(OX_2)^-$ giving negative z_O makes the shape of the wave higher in height and narrower in the width than that of the ideal Nernstian as shown by curve (e) in Figure 4.3(B). Such voltammetric behaviors were experimentally obtained for an Au electrode coated with a monolayer of alkylthiol derivatives of ferrocene, where voltammograms having FWHM narrower than 90.6 mV were obtained and the binding of 3-18 % excess of electrolyte anions (ClO_4^-) to surface-confined ferricinium cations was suggested by EQCM studies [11].

Figure 4.4 shows electrostatic potentials of ϕ_M, ϕ_{PET}, and, ϕ_F (vs. ϕ_S) as a function of applied electrode potentials E (vs. E_{pzc}) for conditions under which voltammograms b, d, and e in Figure 4.3 (B) are obtained. As shown in Figure 4.4 (B), if positive charges generated at PET are almost neutralized by the ion-pairs formation, the magnitude of ϕ_M-ϕ_{PET}, which determines the

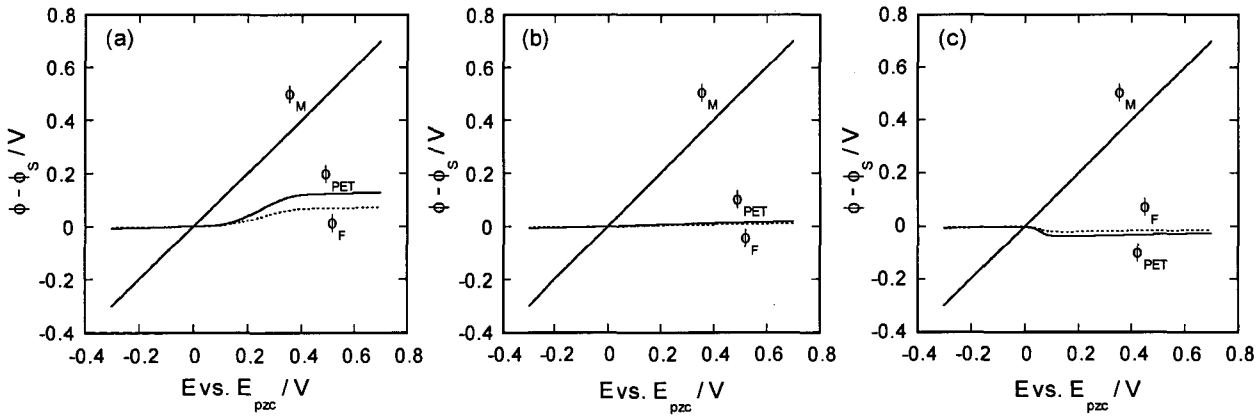

Figure 4.4

Electrostatic potentials, $\phi_M(=\phi(0))$, $\phi_{PET}(=\phi(d_1))$, and $\phi_F(=\phi(d_1+d_2))$ as a function of the applied electrode potential (vs E_{pzc}). Γ_T=3x10^{-10} mol cm^{-2}, (a) K_{o1}=1, K_{o2}=0, z_O=+0.5, (b) K_{o1}=100, K_{o2}=0, z_O =+0.01, and (c) K_{o1}=100, K_{o2}=0.25, z_O =-0.19. Other parameters are given in the text.

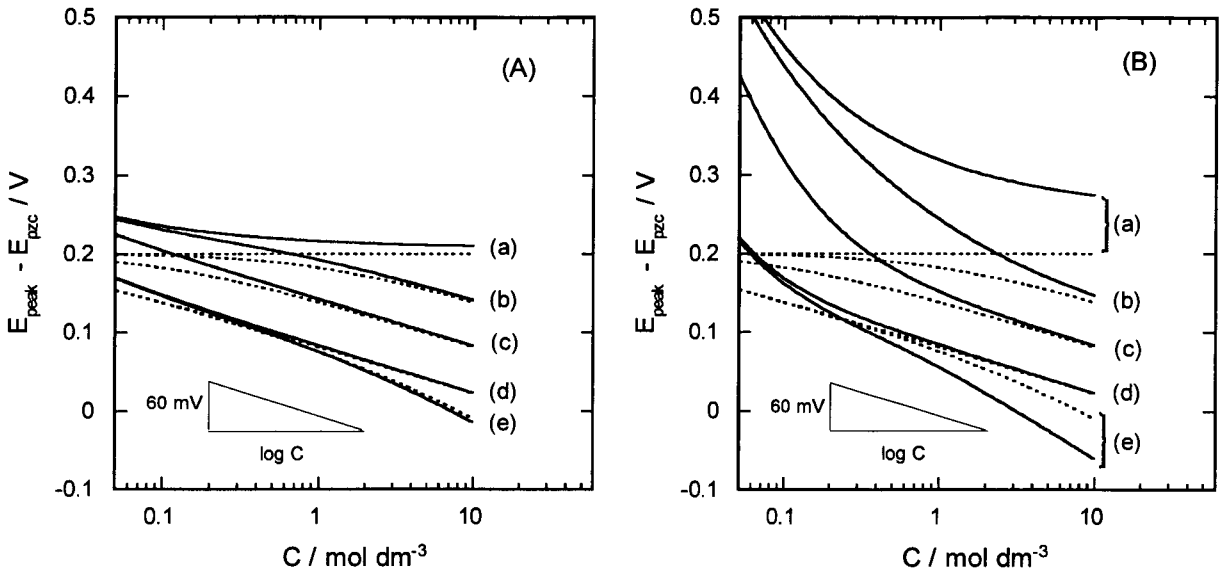

Figure 4.5

Dependence of the voltammetric peak potential (vs E_{pzc}) on the concentration of electrolyte solution. (A) Γ_T=0.3x10^{-10} mol cm^{-2} and (B) Γ_T=3x10^{-10} mol cm^{-2}. (a) K_{o1}= K_{o2}=0, z_O=+1, (b) K_{o1}=1, K_{o2}=0, z_O=+0.5, (c) K_{o1}=10, K_{o2}=0, z_O=+0.09, (d) K_{o1}=100, K_{o2}=0, z_O=+0.01, (e) K_{o1}=100, K_{o2}=0.25, z_O=-0.19. Solid curves are obtained using eq (4.31) and dotted curves are obtained by calculation with use of E_{peak}-E_{pzc}=$E^{o'}$-E_{pzc}+(RT/F)ln(K'), i.e., the double-layer effect is taken into account for the solid curves but not for dotted curves which are the same between Figures 4.5 (A) and 4.5 (B). Other parameters are given in the text.

equilibrium state of surface-confined redox species (see eqs (4.16) and (4.17)), is close to the applied electrode potential (E-E_{pzc}). Then, the shape of the voltammogram is almost the same as that of the ideal Nernstian voltammogram. However, if the positive charges at PET are insufficiently compensated, the value of ϕ_M-ϕ_{PET} is smaller than the applied electrode potential for E>E_{pzc} where the oxidation reaction takes place, as shown in Figure 4.4 (A). Then, an excess polarization is necessary to complete the oxidation, resulting in enlargement of the width of the voltammetric wave. On the contrary, since the formation of triple ions makes the value of ϕ_M-ϕ_{PET} larger than the applied electrode potential as shown in Figure 4.4 (C), the oxidation is accomplished with small polarization, resulting in decrease in FWHM of voltammetric waves from 90.6 mV.

The peak potential (E_{peak}) is influenced by the concentration of electrolyte solutions, because eq (4.31) contains electrolyte concentration-dependent variables of K' given by eq (4.18) and the Debye-Hückel reciprocal length κ(=$zF(2C/\varepsilon_3\varepsilon_0RT)^{1/2}$). Figure 4.5 shows the dependence of the peak potential on the concentration of the electrolyte solution for two different surface concen-

trations of 3.0×10^{-11} and 3.0×10^{-10} mol cm^{-2}. Results for the case of the ideal Nernstian, in which the formation of ion-pairs and triple ions is taken into account but the double-layer effect is not, are also contained in this figure with dotted curves for comparison. Considering that the difference in E_{peak} between the solid curves and the corresponding dotted curves results from the double-layer effect, the deviations of E_{peak} from the ideal Nernstian is not great if the surface concentration of surface-confined redox species is relatively small as shown in Figure 4.5 (A). The dependence with the slope of roughly -60mV/log$C$ appear in that case for low concentrations. In contrast, as shown in Figure 4.5 (B), the deviation from the ideal Nernstian behavior is remarkable at an electrode having a high surface concentration of the redox species unless the charge compensation is complete (curve (d) in Figure 4.5 (B)). According to the results obtained by voltammetric studies on SAM having the ferrocene group, the shifts of E_{peak} with one decade increase of the concentration of perchlorate were 54-60 mV for both cases of relatively low surface density (2.4×10^{-11} mol cm^{-2}) [3] and high density (5.4×10^{-10} mol cm^{-2}) [5]. The results seem reasonable, because the strong ion-pairing must occur between the surface-confined ferricinium cation and perchlorate anion in those cases [5], resulting in complete neutralization of surface charges as given by curve (d) of both Figures 4.5 (A) and (B). To our knowledge, no experimental results have been reported on the relationships between the peak potential and the concentration of the supporting electrolyte solution for cases where electrolyte ions are weakly bound to electrodes having high surface concentration of redox species.

4.3.2 Significance of Present Work in Reference to the Preceding Work

As already shown, the peak current ($i_{f,peak}$) and the peak potential (E_{peak}) are given by eqs (4.30) and (4.31), respectively. Both equations contain a common term of $\varepsilon_1 d_2/(\varepsilon_2 d_1)+\varepsilon_1/(\varepsilon_3 \kappa d_1)$, but this term may be too small to make a significant contributions to the calculated results. If this term is ignored, eqs (4.30) and (4.31) can be simplified

$$i_{f,peak} = \frac{F^2 A v \Gamma_T}{4RT + (z_O - z_R) F^2 \Gamma_T \left(\frac{d_2}{\varepsilon_2 \varepsilon_0} + \frac{1}{\varepsilon_3 \varepsilon_0 \kappa} \right)} \tag{4.33}$$

$$E_{peak} = E^{o} - \frac{RT}{F}\ln\left(1 + CK_{o1} + C^2 K_{o1}K_{o2}\right) + \frac{(z_O + z_R)F\Gamma_T}{2}\left(\frac{d_2}{\varepsilon_2\varepsilon_0} + \frac{1}{\varepsilon_3\varepsilon_0\kappa}\right) \quad (4.34)$$

Such simplification is acceptable for aqueous media having a high ε_3 value, but it may cause serious errors for nonaqueous electrolyte solution systems of low ε_3. The eqs (4.33) and (4.34) have similar forms to eqs (4.35) and (4.36) which were already derived using adjustable parameters [14,15],

$$i_{f,peak} = \frac{F^2 A\Gamma_T v}{4RT - \Gamma_T RT(r_O + r_R)} \quad (4.35)$$

$$E_{peak} = E^{o} - \frac{RT\Gamma_T(r_O - r_R)}{2F} \quad (4.36)$$

where r_O and r_R are so-called interaction parameters which were originally introduced using the Frumkin isotherm to explain an activity effect due to interactions of adsorbed species. However, these equations were derived by assuming that no electrolyte ions are involved in the redox reactions of the surface-confined species. Furthermore, the nature of the interactions itself is not clear, though it may be imagined that purely electrostatic interactions are operative among the surface-confined redox species. The physical significance of the interaction parameters, r_O and r_R in eqs (4.35) and (4.36), can be clarified by correlating the set of eqs (4.33) and (4.34) with the set of eqs (4.35) and (4.36).

$$r_O = -\frac{z_O F^2}{RT}\left(\frac{d_2}{\varepsilon_2\varepsilon_0} + \frac{1}{\varepsilon_3\varepsilon_0\kappa}\right) + \frac{1}{\Gamma_T}\ln\left(1 + CK_{o1} + C^2 K_{o1}K_{o2}\right) \quad (4.37)$$

$$r_R = \frac{z_R F^2}{RT}\left(\frac{d_2}{\varepsilon_2\varepsilon_0} + \frac{1}{\varepsilon_3\varepsilon_0\kappa}\right) - \frac{1}{\Gamma_T}\ln\left(1 + CK_{o1} + C^2 K_{o1}K_{o2}\right) \quad (4.38)$$

According to the original interpretation of the interaction parameters, positive and negative sign of r_O+r_R means attractive interaction and repulsive interaction, respectively, and the peak width of voltammetric waves (i.e., FWHM) is determined by the sign and the magnitude of $(r_O+r_R)\Gamma_T$ [32]. which is obtained with the use of eqs (4.37) and (4.38).

$$(r_O + r_R)\Gamma_T = \frac{F^2(z_R - z_O)\Gamma_T\left(\frac{d_2}{\varepsilon_2\varepsilon_0} + \frac{1}{\varepsilon_3\varepsilon_0\kappa}\right)}{RT} \tag{4.39}$$

In the case of z_R=0, only z_O determines the polarity of r_O+r_R, and if z_O>0 at z_R=0 the charge compensation of the cationic species at PET by electrolyte anions is insufficient, resulting in operation of repulsive forces between the surface-confined cationic species. On the other hand, if triple ions are formed at PET the resulting charges give z_O<0, which favors stabilization of cationic species due to operation of the attractive forces.

It is of importance to note that the numerator of the right hand side of eq (4.39) gives the electrostatic potential energy difference at the PET between f=0 and f=1. In other words, the voltammetric peak width depends on the electrical parts of electrochemical potential but not on the chemical potential. On the other hand, eq (4.34) predicts that the voltammetric peak position changes depending on both the changes of the chemical potential due to the formation of ion-pairs and triple ions (the second term of eq (4.34)) and on the self-atmosphere potential of the PET which stems from σ_{PET} at f=0.5 only (the third term of eq (4.34)).

4.3.3 Estimation of ϕ_{PET} in Real System

As described in the previous section, the potential difference between ϕ_M-ϕ_{PET} and E-E_{pzc} is responsible for non-ideal voltammetric behaviors. If the non-ideal voltammetric behaviors could be explained by such double-layer effects alone, an average potential at PET in real systems can be estimated from knowledge on the fraction of surface-confined species in the oxidized state or reduced state in the following way.

The fraction of surface-confined species in the oxidized state $f(E)$ is obtained from faradaic current i_f as a function of the applied electrode potential E (vs.E_{pzc}).

$$f(E) = \frac{1}{vFA\Gamma_T}\int_{E_{in}}^{E} i_f dE \tag{4.40}$$

where E_{in} is an initial potential in the measurements of voltammograms which must be chosen to be $f(E_{in})=0$. Computational calculations allow the integration of the right hand side of eq (4.40) to determine $f(E)$. On the other hand, f can also be obtained as a function of $\phi_M-\phi_{PET}$ - $(\phi_M-\phi_{PET})_{f=0.5}$ from eq (4.17) without any knowledge of the dielectric constants and the thickness of electrical double-layer, where $(\phi_M-\phi_{PET})_{f=0.5}$ is $\phi_M-\phi_{PET}$ at $f=0.5$ and is equal to $E^o-E_{pzc}-(RT/F)\ln(1+CK_{o1}+C^2K_{o1}K_{o2})$. Of course, the ion-pairing of the reduced species must be considered, if necessary. Figure 4.6 (A) shows f relative to $E-E_{pzc}$ and $\phi_M-\phi_{PET}$ - $(\phi_M-\phi_{PET})_{f=0.5}$. Since $E-E_{pzc}$ and $\phi_M-\phi_{PET}$ - $(\phi_M-\phi_{PET})_{f=0.5}$ having the same f value must have one-to-one correspondence, we can obtain relative relationships between these two parameters as shown in Figure 4.6 (B) with the unit given by the left axis of ordinates. The origin of the relationship is determined with the use of the relation that $\phi_M-\phi_{PET}$ $(=(\varepsilon_1\varepsilon_0\sigma_M)/d_1)$ is 0 at $E=E_{pzc}$. A dotted line in Figure 4.6 (B) is drawn through the origin with the slope of 1 , and ϕ_{PET} relative to the potential of the bulk solution at a given E can be deduced then from the difference in the ordinate between the solid curve and dotted line. Furthermore, the value of $\phi_M-\phi_{PET}$ which is a function of $E_{peak}-E_{pzc}$ gives the formal potential corrected for the double-layer effect. Thus, the Frumkin effect (or ϕ_2-effect) in the real systems can be evaluated quantitatively

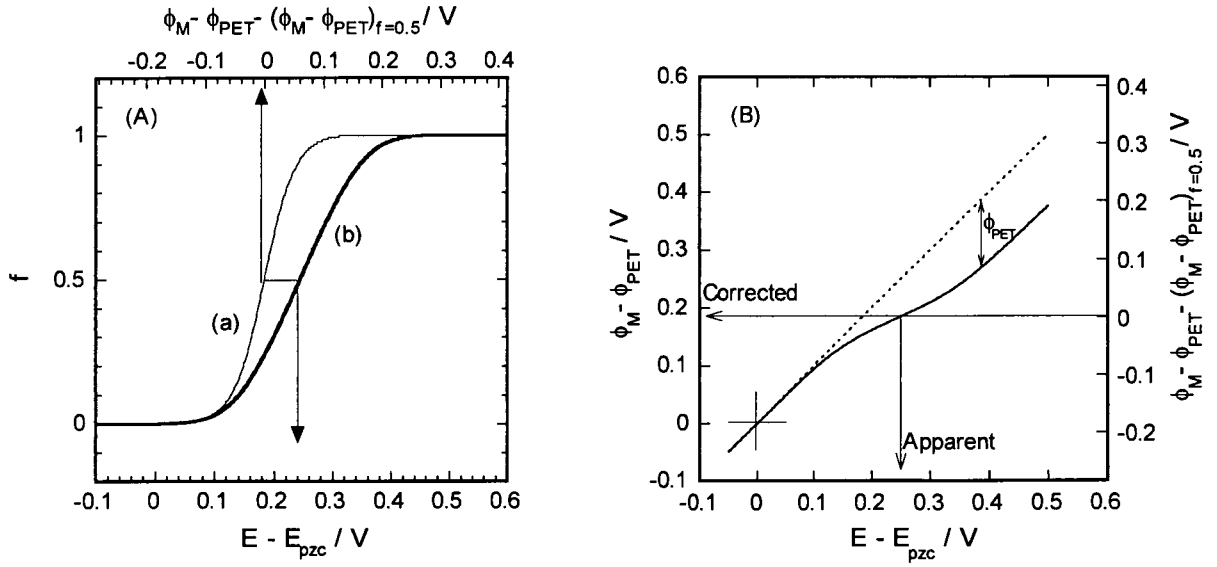

Figure 4.6

The graphical method for estimation of average local potential. (A):curve (a) is for f vs. $(\phi_M-\phi_{PET})-(\phi_M-\phi_{PET})_{f=0.5}$ obtained using eq (4.17) and curve (b) for f vs. $(E-E_{pzc})$ which is obtained by converting the experimentally obtained voltammogram using eq (4.49). (B): solid curve is for $(\phi_M-\phi_{PET})$ vs. $(E-E_{pzc})$ obtained from the one-to-one correspondence of Figure 4.6 (A), and dotted line for $(\phi_M-\phi_S)$ vs. $(E-E_{pzc})$.

from knowledge on the fraction of a surface-confined redox species in either oxidized or reduced state.

4.4 APPENDIX; Gouy-Chapman Model

If the potential drop within the organic layer is too small to be approximated by the potential in the diffuse layer which is given by eq (4.6), the potential distribution must be governed by the Gouy-Chapman model [13]

$$\tanh\left[\frac{zF(\phi(x)-\phi_S)}{4RT}\right]=\tanh\left[\frac{zF(\phi_F-\phi_S)}{4RT}\right]\exp[\kappa(d_1+d_2-x)]\quad x\geq d_1+d_2 \qquad (4A\text{-}1)$$

If this is the case, the same mathematical treatments as those described in the text can be applied and the following relations are obtained.

$$\phi(x)=\left(\frac{d_1+d_2-x}{\varepsilon_2\varepsilon_0}\right)(\sigma_M+\sigma_{PET})+\phi_F \qquad d_1+d_2\geq x\geq d_1 \qquad (4A\text{-}2)$$

$$\phi(x)=\frac{(d_1-x)\sigma_M}{\varepsilon_1\varepsilon_0}+\frac{d_2(\sigma_M+\sigma_{PET})}{\varepsilon_2\varepsilon_0}+\phi_F \qquad d_1\geq x\geq 0 \qquad (4A\text{-}3)$$

where ϕ_F is given by

$$\phi_F=\frac{2RT}{zF}\sinh^{-1}\left[\frac{zF(\sigma_M+\sigma_{PET})}{2RT\varepsilon_3\varepsilon_0\kappa}\right] \qquad (4A\text{-}4)$$

The faradaic currents in that case are given by the use of the following relation instead of eq (4.26)

$$\frac{d\sigma_M}{dE}=\frac{1}{\left(\frac{d_1}{\varepsilon_1\varepsilon_0}+\frac{d_2}{\varepsilon_2\varepsilon_0}\right)+\frac{S}{\varepsilon_2\varepsilon_0\kappa}+\frac{(z_O-z_R)F^2\Gamma_T\left\{\frac{d_2}{\varepsilon_2\varepsilon_0}+\frac{S}{\varepsilon_2\varepsilon_0\kappa}\right\}\left(\frac{d_1}{\varepsilon_1\varepsilon_0}\right)K'e^{\eta}}{RT\left(1+K'e^{\eta}\right)^2}} \qquad (4A\text{-}5)$$

where $S = \frac{1+u(u^2+1)^{-1/2}}{u+(u^2+1)^{1/2}}$ and $u = \frac{zF(\sigma_M + \sigma_{PET})}{2RT\varepsilon_3\varepsilon_0\kappa}$

At the limit of u to 0, eq (4A-5) becomes eq (4.26).

4.5 REFERENCES

1. C.E.D. Chidsey, C.R.Bertozzi, T.M.Putvinski, and A.M.Mujsce, *J. Am. Chem. Soc.*, **112**(1990)4301.
2. H.C. Acevedo and H.D.Abruna, *J. Phys. Chem.*, **95**(1991)9590.
3. G.K. Rowe and S.E.Creager, *Langmuir*, **7**(1991)2307.
4. C.E.D. Chidsey, *Science*, **251**(1991)919.
5. K.Uosaki, Y. Sato, and H. Kita, *Langmuir*, **7**(1991)1510.
6. H.O.Finklea and D.D.Hanshew, *J. Am. Chem. Soc.*, **114**(1992)3173.
7. G.K.Rowe and S.E. Creager, *J. Phys. Chem.*, **98**(1994)5500.
8. S.E. Creager and G.K. Rowe, *J. Electroanal. Chem.*, **370**(1994)203.
9. H.O.Finklea and M.S. Ravenscroft, *J. Phys. Chem.*, **98**(1994)3843.
10. G.K.Rowe, M.T. Carter, J.N. Richardson, and R.W. Murray, *Langmuir*, **11**(1995)1797.
11. K. Shimazu, I. Yagi, Y. Sato, and K. Uosaki, K. *J. Electroanal. Chem.* **372**(1994)117.
12. H.C.D. Long and D.A. Buttry, *Langmuir*, **6**(1990)1319.
13. A.J. Bard and L.R. Faulkner, *Electrochemical Methods*, ; J. Wiley: New York, 1980; Chapter 12.
14. E. Laviron, *J. Electroanal. Chem.*, **52**(1974)395.
15. A.P.Brown and F.C. Anson, *Anal Chem.*, **49**(1977)1589.
16. H. Matsuda, K. Aoki, and K. Tokuda, *J. Electroanal. Chem.*, **217**(1987)15.
17. C.P.Smith and H.S.White, *Anal. Chem.*, **64**(1992)2398.
18. W.R. Fawcett, *J. Electroanal. Chem.*, **378**(1994)117.
19. R. Andreu and W.R. Fawcett, *J. Phys. Chem.*, **98**(1994)12753.
20. C.P. Smith and H.S.White, *Langmuir*, **9**(1993)1.

21. W.R. Fawcett, M.Fedurco, and Z. Kovacova, *Langmuir*, **10**(1994)2403 .

22. X. Gao, H.S. White, S. Chen, and H.D. Abruna, *Langmuir*, **11**(1995)4554.

23. D.C. Grahame, *Chem. Rev.*, **41**(1947)441.

24. I. Rubinstein, In *Physical Electrochemistry*; I. Rubinstein Ed.; Marcel Dekker: New York, 1995; Chapter 1.

25. R.M. Fuoss and C.A. Kraus, *J. Am. Chem. Soc.*, **55**(1993)21.

26. R.M. Fuoss and C.A. Kraus, *J. Am. Chem. Soc.*, **55**(1993)1019.

27. R.M. Fuoss and C.A. Kraus, *J. Am. Chem. Soc.*, **55**(1993)2387.

28. R.M. Fuoss and C.A. Kraus, *J. Am. Chem. Soc.*, **55**(1993)3614.

29. A. Ralston and P. Rabinowitz, *A First Course in Numerical Analysis*; McGraw-Hill: New York, 1965; Chapter 8.

30. C. Miller, P. Cuendet, and M.Gratzel, *J. Phys. Chem.*, **95**(1991)877.

31. J.O'M.Bockris, M.A.V. Devanathan, and K.Muller, *Proc. Roy. Soc.* **A274**(1963)55.

32. D.F. Smith, K. William, K. Kuo, and R.W. Murray, *J. Electroanal. Chem.*, **95**(1979)217.

Conclusion

This thesis has dealt with novel functionalized electrodes prepared by utilizing self-assembled monolayer and with theoretical treatments of voltammetric behaviors of electrodes coated with self-assembled monolayer. The main results and conclusions obtained in this study are summarized as follows.

Chapter 1 describes the preparation of a microelectrodes array utilizing photo-induced elimination of hexadecylthiolate on Au electrode. An electrode characteristics of a microelectrodes array was fabricated by irradiating with UV lights of a self-assembled monolayer of hexadecylthiolate formed on Au electrode in air through a photomask. Furthermore, it was discovered that the irradiation of the monolayer electrode in a $K_4Fe(CN)_6$ solution allowed removal of the monolayer in such a way asto give an electrode characteristics of microelectrodes array depending on irradiation time. A microelectrodes array was also fabricated by irradiating the monolayer electrode with focused laser beam of the second harmonics of a Nd:YAG laser (532 nm) in ordered places in a $K_4Fe(CN)_6$ solution. Cyclic voltammograms of the photo-fabricated electrodes are compared with those predicted from voltammetric theories.

Chapter 2 describes the preparation of a microelectrodes array utilizing elimination of hexadecylthiolate on Au electrode in cyanide solution. The immersion of an Au electrode coated with a self-assembled monolayer of hexadecylthiolate (HDT/Au) in KCN aqueous solution causes desorption of chemisorbed hexadecylthiolate molecules, depending on the immersion time. The desorption is initiated at pinholes of the HDT/Au electrode through which cyanide ions reach the gold substrate, causing desorption of the adsorbed hexadecylthiolate. Electrochemical deposition of copper onto the HDT/Au electrode after immersing the electrode in KCN solution revealed that the size of holes generated by desorption of the adsorbed hexadecylthiolate became large as the immersion time in the KCN solution increased, and the holes produced were distributed fairly homogeneously over the entire surface of the HDT/Au electrode. Detailed simulations of cyclic voltammograms of the HDT/Au electrode obtained in $K_4[Fe(CN)_6]$ solutions after immersing the

electrode in the KCN solution suggested that the resulting electrodes possessed electrochemical activities characteristics of a microelectrode array depending on the immersion time in the cyanide solution. The average radius of the microelectrodes estimated by the best fitting of the experimentally obtained voltammograms to the simulated ones accorded well with that obtained from observations of the Cu-deposited electrode by an optical microscope.

Chapter 3 describes the utilization of self-assembled monolayer as an anchor to attach functional molecules onto electrode surface. Au wire electrodes coated with phenothiazine derivatives such as thionine, azure C, and azure A were covalently bound to self-assembled monolayer of 3,3'-dithiobis(succineimidylpropionate) on the Au substrate, and the resulting electrodes showed two redox waves due to monomeric and dimeric forms of the phenothiazine derivatives. It was found that the dimeric forms have high activities for electrocatalytic oxidation of NADH. The second-order reaction rate constant for NADH oxidation was evaluated by digital simulation. The rate constants obtained at the thionine-modified electrodes was about 10^4 times greater than that obtained for the oxidized phenothiazine derivatives dissolved in solution, and was greater than those reported previously with use of other electrocatalysts.

Chapter 4 describes a theory on voltammetry of electrodes coated with electroactive monolayer film. Potential distribution at electrode/solution interface is discussed for a metal electrode coated with a self-assembled monolayer containing redox active moieties with taking into consideration of inclusion of ion-pairs and triple ions formation. Theory on current-voltage curves in a potential sweep experiments is derived for these special cases. Explicit expressions derived in this study for the peak current and the peak potential have similar in their forms to those published previously using the Frumkin adsorption isotherm. Methods to graphically evaluate the average local potential in the double layer of the real system are proposed. The results derived here does not require the use of adjustable parameters in obtaining the peak current and the peak potential in cyclic voltammograms, and can explain well the appearance of currents spikes and broadning of the waves of voltammograms.

Acknowledgment

The work of this thesis was carried out under the guidance of Professor Dr. Hiroshi Yoneyama at Department of Applied Chemistry, Faculty of Engineering, Osaka University. I would like to express grateful acknowledgment to Professor Dr. Hiroshi Yoneyama for his continuous guidance and encouragement throughout this work. I am also indebted to Professor Dr. Shun-ichi Fukuzumi for his helpful comments and suggestions. I am very grateful to Associate Professor Dr. Susumu Kuwabata for his expert suggestions and comments. And many thanks to my co-worker, Mr. Tomohide Sunagawa for his contribution in preparing this work. I must also acknowledge the provocative and productive environment of the Yoneyama Laboratory —— discussions with Dr. Matsuhiko Nishizawa, Dr. Tsukasa Torimoto, and Mr. Sinpei Kado —— encouragement by younger students. Finally, I offer simple thanks to my family for affording me time for this endeavor.

M.Ohtani